Impact of wildfire smoke on Arctic cirrus formation, part 2: simulation of MOSAiC 2019-2020 cases

Albert Ansmann[1], Cristofer Jimenez[1], Daniel A. Knopf[2], Johanna Roschke[1], Johannes Bühl[1,3], Kevin Ohneiser[1], and Ronny Engelmann[1]

[1]Leibniz Institute for Tropospheric Research, Leipzig, Germany
[2]School of Marine and Atmospheric Sciences, Stony Brook University, Stony Brook, NY 11794, USA
[3]Harz University of Applied Sciences, Wernigerode, Germany

Correspondence: A. Ansmann
(albert@tropos.de)

Abstract.

A simulation study on the impact of wildfire smoke (aged organic aerosol particles) on cirrus formation in the central Arctic is presented. The simulations in this part 2 of a series of two articles complement the MOSAiC (Multidisciplinary drifting Observatory for the Study of Arctic Climate) field observations, presented and discussed in part 1. The measurements were

5 performed with lidar and radar aboard the ice breaker Polarstern at latitudes $> 85°$N during the winter half year 2019-2020. Main goal of the MOSAiC data analysis in part 1 was to gather a consistent set of indications for an impact of the observed aged Siberian wildfire smoke on the formation of embedded ice clouds. The combination of (a) mostly low ice crystal number concentration (ICNC) of 0.1-10 L^{-1} in almost all of the observed cirrus cloud virga, pointing to heterogeneous ice nucleation, (b) typically high ice saturation ratios in the upper part of the analyzed cirrus systems of around 1.3–1.4, and (c) significantly

10 enhanced levels of smoke pollution characterized by particle surface area concentrations of the order of 5-15 μm^2 cm^{-3} corroborate our hypothesis that wildfire smoke particles served as ice nucleating particles (INPs) in Arctic cirrus with typical cloud top temperatures of -60 to $-75°$C. The observed high ice saturation ratios suggest relatively inefficient ice-active aerosol particles, as expected in the case of wildfire smoke. Main goal of the simulations in part 2 is to gain a deeper insight into the potential smoke influence on cirrus formation as a function of aerosol and meteorological conditions (temperature, relative

15 humidity) and by considering realistic gravity wave characteristics (updraft speed, wave amplitude). The modeling effort uses lidar-derived values of INP number concentration as input and ICNC values retrieved from combined lidar-radar observations for comparison with the simulation results. The model allows us to simulate adiabatic lofting of air parcels triggered by gravity waves, nucleation of ice crystals on smoke particles (deposition ice nucleation), homogeneous freezing of background aerosol particles, the growth of the nucleated ice particles by deposition of water vapor on the crystals, and sedimentation effects.

20 Observations of meteorological state parameters (temperature, relative humidity) with four radiosondes per day and of the aerosol and cirrus properties from continuous lidar and radar profiling permitted a realistic model-based investigation of the smoke influence on Arctic cirrus evolution. The simulations confirm that the smoke INPs were able to suppress homogeneous freezing of background aerosol particles and to trigger ice nucleation at high ice saturation ratios of 1.3–1.5 over the North Pole region at cirrus top temperatures mostly $< -60°$C. The simulations further reveal that shallow gravity waves with amplitudes

25 of the order of < 100 m and the comparably low ice nucleation efficiency of the smoke INPs provided favorable conditions for the evolution of thin ice clouds with low ICNC as observed.

1 Introduction

The MOSAiC (Multidisciplinary drifting Observatory for the Study of Arctic Climate) expedition (Shupe et al., 2022) offered the unique opportunity to investigate the impact of wildfire smoke on cirrus formation. Smoke-cirrus interaction is an important

30 pathway for smoke to sensitively influence weather and climate. Little is known about the potential of smoke to serve as ice nucleating particles (INPs) in heterogeneous ice nucleation processes in the upper troposphere at low temperatures of $< -50°$C. During the one year MOSAiC campaign from October 2019 to September 2020, aged Siberian wildfire smoke covered the central Arctic during the first 7.5 months (October 2019 to mid-May 2020) (Ohneiser et al., 2021; Ansmann et al., 2024b)

In part 1 (Ansmann et al., 2024a), we presented our measured MOSAiC cirrus and smoke products, retrieved from contin-

35 uously operated lidar and cloud radar instruments aboard the research ice breaker Polarstern, with the goal to provide clear observational evidence for an impact of aged wildfire smoke (organic aerosol particles) on cirrus formation in the central Arctic during the winter half year of 2019-2020. The observed combination of (a) low ice crystal number concentration (ICNC) of 0.1-10 L^{-1} in most of the analyzed 20 cirrus events, pointing to the dominance of heterogeneous ice nucleation and (b) the high ice saturation ratios, accumulating around 1.3-1.4 at cirrus top height level, in (c) the presence of significantly elevated levels

40 of smoke aerosol pollution (showing particle surface area concentrations of typically 5-15 μm^2 cm^{-3}) are in consistency with our hypothesis that wildfire smoke particles, expected to be inefficient INPs (Kanji et al., 2008; Wang and Knopf, 2011; Knopf et al., 2018), were able to serve as INPs in Arctic cirrus formation processes at high super saturation levels and low cirrus top temperatures of $-60°$ to $-75°$C. Besides the background and volcanic sulfate aerosol (causing homogeneous freezing) the only further aerosol type present in the upper troposphere over the central Arctic in the winter of 291-2020 was definitely aged

45 wildfire smoke (Ohneiser et al., 2021; Ansmann et al., 2024b).

The simulations in this part 2 complement the MOSAiC field observations in part 1. The modeling effort is based on MOSAiC aerosol, cirrus, and meteorological observations. Main goal of the simulations is to reproduce the retrieved MOSAiC ICNC values for the observed Arctic environmental and meteorological conditions, and to gain in this way a more detailed insight into the impact of wildfire smoke and given meteorological conditions on cirrus formation. The focus is on the onset of

50 ice nucleation in an adiabatically ascending air parcel, e.g., during the updraft phase of a gravity wave. Besides heterogeneous nucleation of ice crystals on smoke INPs (aged organic aerosol particles), homogeneous freezing of the omnipresent liquid background aerosol particles and the growth of nucleated ice particles by deposition of water vapor on the crystals is simulated. Sedimentation of ice crystals is considered as well. Crystal growth is an essential part of the simulations and able to terminate ice nucleation events in ascending air parcels. The basic design of the model widely follows the simulation concept of Kärcher

55 et al. (2022).

In our specific approach, INP number concentration (INPC) and ICNC are treated in a prognostic fashion. This means we account for sources and sinks of INPs and ice crystals in the ascending air parcel as discussed in detail by Knopf et al. (2023a).

The smoke particles are considered as the source of INPs. Once the INPs activate and form ice crystals, these INPs are removed from the INP reservoir (sink of INPs). The source of ice crystals are the activated INPs. Ice crystal growth and subsequent sedimentation removes ice crystals from the air parcel (sink of ice crystals). Cirrus formation scenarios exhibit various updraft periods (of different temporal length, velocity strength, and vertical extent), caused by windshear-induced turbulence and gravity wave activity. To account for the time-dependence of ice nucleation, ice crystal growth and removal processes, taking place simultaneously, we chose an ice nucleation parameterization based on classical nucleation theory (CNT) (Knopf and Alpert, 2023). In CNT, the heterogeneous ice nucleation rate coefficient, J_{het} in units of cm^{-2} s^{-1}, describes the number of ice nucleation events per particle surface area and time. Multiplication with particle surface area yields an ice nucleation rate in units of s^{-1}, ultimately determining the number of ice nucleation events, i.e., ice crystal number concentration per modeling time step. Another feature of our model is that we assume that the INP reservoir consists of all available smoke particles with radius >250 nm. This means that all smoke particles of the large-particle fraction are potentially activatable INPs. Here, we follow the argumentation given in Knopf et al. (2023a). We selected a high temporal resolution of one second in the simulations. This high resolution is required to adequately resolve the burst-like ice nucleation events.

The simulations make use of (1) the observed aerosol properties such as the aerosol particle surface area concentration (PSAC), which serves as the aerosol input parameter in the ice nucleation computation, (2) of retrieved ICNC values in the cirrus virga (Ansmann et al., 2024a), for comparison with the simulation results, and (3) a dense set of MOSAiC radiosonde observations of temperature and relative humidity profiles (Maturilli et al., 2021, 2022). Four radiosonde launches per day were performed throughout the entire MOSAiC year from October 2019 to September 2020. The article is organized as follows: in Sect. 2, we provide details of the simulation model. In Sect. 3, we present the key findings of the simulations. A brief summary of the simulations and conclusions on smoke-cirrus interaction are provided in Sects. 3.5 and 4.

2   Simulation model

The main structure of the simulation model is presented in Fig. 1. A smoke-filled air parcel is ascending adiabatically (blue arrows and boxes in Fig. 1) so that temperature T decreases with 0.00984 K m^{-1}. The decrease of air pressure p is obtained by applying the barometric formula. The simulated vertical movements may be triggered by gravity waves (Haag and Kärcher, 2004; Spichtinger et al., 2005; Kärcher and Podglajen, 2019). Updraft speeds are typically in the range from 0.05 to 1 m s^{-1}. During the adiabatic ascent the water vapor mixing ratio MR remains constant. As shown in Fig. 1 (red boxes), we consider ice nucleation, growth of freshly nucleated and existing ice crystals (nucleated in the computational steps before), and heat release during ice crystal growth. We widely follow the modeling concept as given in recent articles of Kärcher et al. (2022, 2023); Spichtinger et al. (2023).

Regarding heterogeneous nucleation of ice crystals on organic aerosol particles (INPC) we apply the deposition ice nucleation (DIN) parameterization (Wang and Knopf, 2011). The method is outlined in Ansmann et al. (2021) for lidar applications. The predicted number concentration of ice crystals (ICNC) is given by:

$$n_{\text{i,het}} = s_{\text{p}} \times J_{\text{het}}(c_{\text{angle}}, T, S_{\text{i}}) \times \Delta t \tag{1}$$
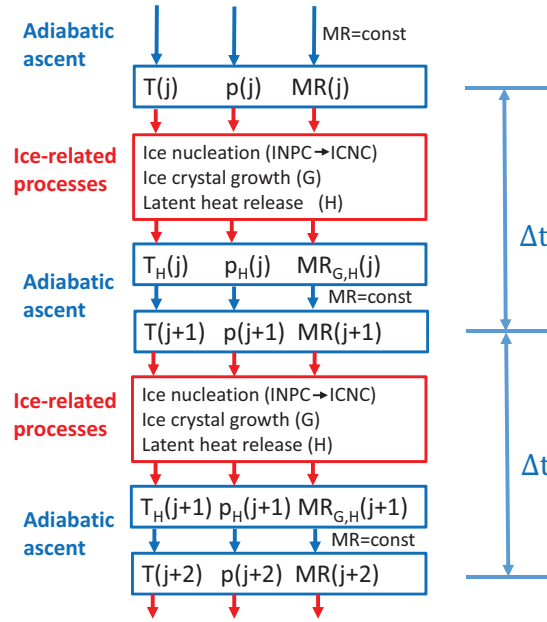
Figure 1. Simulation model to study the initial stage of cirrus formation during an adiabatic lofting event. Controlling meteorological input parameters are the air temperature T, air pressure p, relative humidity RH and water vapor mixing ratio MR. Adiabatic rise of air parcels is indicated by blue arrows and boxes. The vertical (range) resolution is defined by the product of vertical velocity and the temporal resolution Δt (of 1 s) in the computation. Computations performed in step j and step $j+1$ are listed. Red boxes and arrows indicate ice nucleation, ice crystal growth, and heat release processes that have an impact on the meteorological conditions. Indices G and H indicate an impact of ice crystal growth and heat release on the different meteorological parameters. Sedimentation aspects are considered by excluding particles with radius $>10\ \mu$m in the growth calculations.

with the smoke particle surface area concentration s_p and the nucleation time interval Δt. The retrieval of s_p from lidar backscatter observations is described in Ansmann et al. (2021, 2023). The nucleation rate coefficient J_het is a function of the contact angle c_angle, ice nucleation temperature T and ice saturation ratio S_i, i.e., the ratio of the partial pressure of water vapor p_w and saturation vapor pressure with respect to ice $p_\mathrm{i,sat}$. The contact angles for organic aerosol are in the range of 22°-30° (Wang and Knopf, 2011). With increasing ice-nucleation efficiency the contact angle decreases. For mineral dust, the contact angle is in the range of 10°-15° (Wang and Knopf, 2011). In the model, the contact angle increases with temperature. The respective ice nucleation onset value $S_\mathrm{i,on}$ is is about 1.25-1.3 for a contact angle of 23.5° at 220 K and 1.45-1.5 for a contact angle of 26.5° at 200 K (Wang and Knopf, 2011; Wang et al., 2012). Regarding the organic material, leonardite (a standard humic acid surrogate material) is assumed to represent the amorphous organic coating of smoke particles. Leonardite, an oxidation product of lignite, is a humic-acid-containing soft waxy particle (mineraloid), black or brown in color, and soluble in alkaline solutions. The INP characteristics of leonardite were studied in detail in laboratory experiments (Kanji et al., 2008; Wang and Knopf, 2011; Knopf and Alpert, 2013; Rigg et al., 2013).

Eq. (1) assumes that all wildfire smoke particles are potential INPs, thus contributing to the INP reservoir (Knopf et al., 2023a). According to the discussion in Sect. 3.2 in Ansmann et al. (2024a), the observed MOSAiC particle surface area

105 concentration (PSAC) was of the order of 10 μm^2 cm^{-3} (Ansmann et al., 2024a), and the total particle number concentration n_{50} (considering all particles with radius > 50 nm) in the range of 50000-100000 L^{-1}. In our simulations, we restricted the INP reservoir to the particle number concentration n_{250} (considering particles with radius > 250 nm), assuming that the large particle fraction contains the most favorable INPs (DeMott et al., 2010). n_{250} is about 2000 L^{-1} for PSAC values of 10 μm^2 cm^{-3}, indicating the maximum size of the INP reservoir. More details to the consideration of the INP reservoir in the

110 simulations is given below.

We also simulate ice nucleation via homogeneous freezing (Koop et al., 2000; Knopf and Rigg, 2011; Schneider et al., 2021):

$$n_{i,hom} = v_{p,bg} \times J_{hom}(T, S_i) \times \Delta t \qquad (2)$$

with the number concentration of homogeneously nucleated ice crystals $n_{i,hom}$, the volume concentration for sulfate back-

115 ground aerosol $v_{p,bg}$, and the ice nucleation rate coefficient J_{hom} which is a function of temperature T, ice saturation ratio S_i (Koop et al., 2000). Here, we assume sulfate particles with radius of 50-100 nm. For computational details in the case of lidar application see Ansmann et al. (2021). A very high ice saturation ratio S_i of 1.5-1.6 is required to initiate homogeneous freezing. All available liquid background aerosol particles can be regarded as INPs (Heymsfield et al., 2017). According to airborne in situ observations of Schröder et al. (2002) the number concentration of background sulfate particles is of the order

120 of 250 cm^{-3} or 250000 L^{-1} in the upper troposphere and the volume concentration $v_{p,bg}$, required in Eq. (2), is 1.0 μm^3 cm^{-3}.

An updated approach to compute $n_{i,hom}$ can be found in Koop and Zobrist (2009). According to previous studies (Knopf and Rigg, 2011; Riechers et al., 2013), J_{hom} in Eq. (2) is probably one to two orders of magnitude too large. However, our simulation show that this overestimation has only a minor impact on $n_{i,hom}$. In the case of Arctic cirrus with ice nucleation temperatures around 200 K the over estimation is of the order of 5%.

125 The concentration of nucleated ice cyrstals is finally given by the sum

$$n_i = n_{i,het} + n_{i,hom}. \qquad (3)$$

The nucleated ice crystals begin to grow by deposition of water vapor on the crystals. This process reduces the water vapor content in the air parcel and thus the ice saturation ratio S_i. If S_i decreases below the ice-nucleation threshold or onset level given by $RH_{i,on}$, ice nucleation will stop. The ice particle mass growth rate (for one crystal) is given by Lohmann et al. (2016)

130
$$\frac{dm_i}{dt} = \frac{4\pi C_i (S_i - 1)}{F_G + F_H}. \qquad (4)$$

When assuming compact spherical ice crystals with radius r_i shortly after nucleation, instead of hexagonal plates or columns, the ice particle capacitance C_i (Westbrook et al., 2008) can be replaced by r_i. According to Skrotzki et al. (2013), this important simplification is justified. When expressing dm_i/dt by $4\pi r_i^2 \rho_i n_i (dr_i/dt)$, we can obtain the increase of the ice crystal particle

size from Eq. (4) (Lohmann et al., 2016):

$$\frac{\mathrm{d}r_\mathrm{i}}{\mathrm{d}t} = \frac{1}{r_\mathrm{i}} \frac{S_\mathrm{i} - 1}{\rho_\mathrm{i}(F_\mathrm{G} + F_\mathrm{H})}. \tag{5}$$

ρ_i is the bulk ice mass density (assumed to be 925 kg m^{-3}).

The term F_G is related to the mass transfer of water molecules to the surface of the crystals (Skrotzki et al., 2013):

$$F_\mathrm{G} = \frac{R_\mathrm{w}T}{D_\mathrm{w}^* p_\mathrm{i,sat}} \tag{6}$$

with the specific gas constant of water vapor $R_\mathrm{w} = 461.5$ J kg^{-1} K^{-1} and the ice saturation pressure $p_\mathrm{i,sat}$. Mass transfer of water molecules to the surface of the ice crystals is considered via the so-called modified version of water vapor diffusivity D_w^* (Skrotzki et al., 2013). D_w^* is given by

$$D_\mathrm{w}^* = D_\mathrm{w} \left(\frac{r_\mathrm{i}}{r_\mathrm{i} + \Delta_\mathrm{w}} + \frac{4D_\mathrm{w}}{\alpha_\mathrm{i} r_\mathrm{i} v_\mathrm{w}} \right)^{-1} \tag{7}$$

with the water vapor diffusivity,

$$D_\mathrm{w} = 2.11 \times 10^{-5} \left(\frac{T}{T_0} \right)^{1.94} \frac{p_0}{p}, \tag{8}$$

where T and p are air temperature and pressure, respectively, and $T_0 = 273$ K and $p_0 = 1013$ hPa. Δ_w in Eq. (7) is the so-called water vapor jump length which is often chosen to be of the order of the mean free path λ_w of the water vapor molecules in air, so that we use $\lambda_\mathrm{w} \approx \Delta_\mathrm{w}$ (Skrotzki et al., 2013). The mean free path λ_w is given by

$$\lambda_\mathrm{w} = k_\mathrm{B}T \left(\pi p \left(\frac{\sigma_\mathrm{w} + \sigma_\mathrm{a}}{2} \right)^2 \sqrt{1 + \frac{M_\mathrm{w,mol}}{M_\mathrm{a,mol}}} \right)^{-1} \tag{9}$$

with the Boltzmann constant k_B, the collision diameters of a water vapor molecule σ_w (about 0.27 nm) and of an air molecule σ_a (about 0.37 nm), and molar mass of water $M_\mathrm{w,mol}$ and of air $M_\mathrm{a,mol}$. In short, $\lambda_\mathrm{w} = 3.371 \times 10^{-5} \times T/p$ with temperature in Kelvin and pressure in Pascal. The thermal velocity in Eq. (7) is given by

$$v_\mathrm{w} = \sqrt{\frac{8R_\mathrm{w}T}{\pi}}, \tag{10}$$

in short $v_\mathrm{w} = 34.28\sqrt{T}$. Finally, the accommodation coefficient or deposition coefficient α_i (Skrotzki et al., 2013) in Eq. (7) must be given as input and is set constant. Reasonable values are 0.5-1.0. Skrotzki et al. (2013) recommended a deposition growth coefficient of 1.0. Kärcher et al. (2022, 2023) introduced a complex scheme to compute α_i as function of crystal size and ice saturation ratio S_i. The approach is based on sophisticated laboratory investigations discussed in the articles. The discussions in Kärcher et al. (2023) emphasizes that further work is needed in this complex field of research. We follow Spichtinger et al. (2023) and set $\alpha_\mathrm{i} = 0.5$.

The thermodynamic term F_H in Eqs. (4) and (5) is related to latent heat release due to the diffusion of heat away from the ice crystal (Lohmann et al., 2016):

$$F_\mathrm{H} = \left(\frac{L_\mathrm{s}}{R_\mathrm{w}T} - 1 \right) \frac{L_\mathrm{s}}{KT} \tag{11}$$

with $L_{\mathrm{s}} = 2.836 \times 10^6$ J kg^{-1} (denoted as heat of sublimation) and

$$K = 4.1868 \times 10^{-3}[5.69 + 0.017(T - 273.15)]. \tag{12}$$

F_{H} contributes to the sum $F_{\mathrm{G}} + F_{\mathrm{H}}$ by <5% for temperatures <235 K and is thus of low importance.

165   In the following, we explain the successive steps in the simulations of the MOSAiC cirrus cases. The starting height z_0 of the simulations is set into the top region of the cirrus (the coldest part of the cloud with highest ice saturation ratio). In the case of a gravity wave, the air parcel will be lofted from z_0 to $z_0 + A_{\mathrm{GW}}$, with the amplitude of the gravity wave A_{GW}, and will then descend to $z_0 - A_{\mathrm{GW}}$ before returning to z_0. We also simulated lofting with constant updraft speed from z_0 to $z_0 + 300$ m. The corresponding meteorological conditions (air pressure p, temperature T, relative humidity RH over water, and corresponding

170   water vapor mixing ratio MR) were taken from the MOSAiC radiosonde data base (Maturilli et al., 2022). The smoke aerosol conditions (e.g., the particle surface area concentration s_{p}) were available from lidar observations before and after the cirrus events (Ansmann et al., 2021, 2024a).

    The temporal resolution in the simulations is set to $\Delta t = 1$ s (see Fig. 1). The height resolution is then, e.g., for 0.2 m in the case of an updraft velocity $v_{\mathrm{up}} = 0.2$ m s^{-1}. In Fig. 1, the calculation steps j and $j + 1$ after exceeding the threshold or onset

175   ice saturation level $S_{\mathrm{i,on}}$ for heterogeneous ice nucleation are shown. As long as the threshold relative humidity RH$_{\mathrm{i,on}}$ is not reached, the simulated air parcel just ascends with the given vertical velocity and n_{i} remains zero.

    The number of ice crystals that nucleated in step j (after exceeding the onset $S_{\mathrm{i,on}}$) is given by $n_{\mathrm{i}}(j)$ (see Eqs. (1)-(3)). All earlier formed ice crystals (formed in the lower layers before, indicated by index l ($l < j$) from 1 to $j - 1$ in Eq. 13 below, with modeling step index j) remain in the air parcel during the entire ascent and permanently grow by water vapor uptake.

180   The consideration of sedimentation aspects is discussed in the last paragraph of the section. The time given for ice crystals, formed in layer l, to grow is $(j - l) \times \Delta t$. This means, the lower the layer (the lower index l), in which ice crystals nucleated, the larger they are according to Eqs. (4) and (5) in the computations of ice mass growth in step $j_{\mathrm{step}} = j$. The ice crystals that were nucleated in the foregoing steps $l = 1$ to $j - 1$ and the freshly nucleated ice crystals in step j increase the mass transfer of water molecules to the surface of atmospheric ice particles within the time interval $\Delta t(j)$ according to (Lohmann et al., 2016;

185   Kärcher et al., 2023). The ice mass $M_{\mathrm{i}}(j)$ produced within the time interval $\Delta t(j)$ (see first red box in Fig. 1) is given by

$$M_{\mathrm{i}}(j) = \frac{4\pi}{3}\rho_{\mathrm{i}}n_{\mathrm{i}}(j)[r_{\mathrm{i}}(j)^3 - r_{\mathrm{INP}}^3]\frac{\Delta t}{2} + \sum_{l=1}^{j-1}\frac{4\pi}{3}\rho_{\mathrm{i}}n_{\mathrm{i}}(l)[r_{\mathrm{i}}(j,l)^3 - r_{\mathrm{i}}(j-1,l)^3]\Delta t. \tag{13}$$

The crystals that nucleated in the last step j are the smallest and had, on average, only the time period of $0.5\Delta t$ to grow. For simplicity, the core mass density of an INP with radius r$_{\mathrm{INP}}$ (set to 0.25 μm) in Eq. (13) is assumed to be equal to ρ_{i}. The increase of the crystal radius $r_{\mathrm{i}}(j)$ with time Δt is computed by using Eq. (5).

190   In the next step, the ice mass $M_{\mathrm{i}}(j)$ that formed during the time interval $\Delta t(j)$ must be subtracted from the absolute humidity (in g m^{-3}) in the air parcel,

$$m_{\mathrm{w}} = \frac{p_{\mathrm{w}}}{R_{\mathrm{w}}T}, \tag{14}$$

to obtain the absolute humidity after ice growth in step j,

$$m_{\mathrm{w,G}}(j) = m_{\mathrm{w}}(j) - M_{\mathrm{i}}(j)\,. \tag{15}$$

195   Furthermore, the heat release resulting from the water vapor deposition on the ice embryos and growing ice crystals, increases the temperature (Spichtinger et al., 2023),

$$T_{\mathrm{H}}(j) = T(j) + M_{\mathrm{i}}(j) \times L_{\mathrm{s}}/c_{\mathrm{p}}\,. \tag{16}$$

The air pressure $p(j)$ is influenced via the dependence of the barometric formula on the ambient temperature $T_{\mathrm{H}}(j)$ so that we introduce $p_{\mathrm{H}}(j)$ in Fig. 1. Then, we step forward and compute the water vapor pressure $p_{\mathrm{w,G,H}}(j)$ after ice growth (index G)

200   and heat release (index H),

$$p_{\mathrm{w,G,H}}(j) = m_{\mathrm{w,G}}(j) \times R_{\mathrm{w}} T_{\mathrm{H}}(j)\,, \tag{17}$$

by using Eq. (14) and the respective water vapor mixing ratio ($\mathrm{MR_{G,H}}$ in Fig. 1)

$$q_{\mathrm{w,G,H}}(j) = 0.622 \frac{p_{\mathrm{w,G,H}}(j)}{p_{\mathrm{H}}(j) - p_{\mathrm{w,G,H}}(j)}\,. \tag{18}$$

The ice saturation ratio, affected by ice crystal growth and related water vapor loss, can be written as (cf. Eq. 15)

205   $$S_{\mathrm{i,G,H}}(j) = \frac{[m_{\mathrm{w}}(j) - M_{\mathrm{i}}(j)] \times R_{\mathrm{w}} T_{\mathrm{H}}(j)}{p_{\mathrm{i,sat}}}\,. \tag{19}$$

Afterwards, the next step of adiabatic lofting is simulated. The water vapor mixing ratio $\mathrm{MR_{G,H}}$ is again constant during this computation of adiabatic lofting.

The simulations consider a limited INP reservoir consisting of smoke particles with radius >250 nm. The respective particle number concentration n_{250} is estimated from the MOSAiC lidar observations in the upper troposphere. If this INP reservoir is

210   depleted, ice nucleation stops. The INP concentration n_{INP}, equivalent to $n_{\mathrm{i,het}}$, is calculated with Eq. (1). The INP reservoir n_{250} is considered via

$$n_{250}(j) = n_{250}(j-1) - n_{\mathrm{i}}(j-1)\,. \tag{20}$$

We assume that the large particles are the most favorable INPs as suggested by DeMott et al. (2010). All of the large particles are potentially available to serve as INP in the simulations. According to the study of Ansmann et al. (2021), which deals with

215   the conversion of lidar-derived particle extinction coefficients (in Mm^{-1}) into microphysical properties such as the surface area concentration s_{p} (in $\mu\mathrm{m}^2\,\mathrm{cm}^{-3}$) and the large particle fraction n_{250} (in cm^{-3}), the link between these two derived properties is given by

$$s_{\mathrm{p}}(j) = \frac{c_{\mathrm{s}}}{c_{250}} \times n_{250}(j) \tag{21}$$

with the ratio of the extinction-to-surface-area conversion factor c_{s} (in $\mathrm{Mm}\,\mu\mathrm{m}^2\,\mathrm{cm}^{-3}$) to the extinction-to-particle-number

220   conversion factor c_{250} (in $\mathrm{Mm}\,\mathrm{cm}^{-3}$). For aged smoke the ratio is 5 $\mu\mathrm{m}^2$ (Ansmann et al., 2021). The factor c_{s}/c_{250} can be

interpreted as the average particle surface area of all particles of the large particle fraction (defined by n_{250}). The new, updated $s_p(j)$ value is used in the next step of $n_i(j)$ calculation with Eq. (1).

We made also an attempt to consider ice crystal sedimentation effects, i.e., the removal of larger ice crystals (with significantly sedimentation speed) from the air parcel under investigation. Particles, that leave the nucleation cells, do no longer

225 contribute to ice growth in these nucleation cells, and thus to the reduction of ice supersaturation. As we will show in the results section, sedimentation processes improve the conditions for new ice nucleation processes during further lofting of the rising air parcels. In our simulation, we simply assume that all particles with $r_i(j) > 10~\mu$m leave the air parcel and are no longer considered in the mass computation with Eq (13). Khvorostyanov and Curry (2005) show that ice crystals with radius of 5, 10, and 15 μm may fall with velocities of 5-10 cm s^{-1}, 10-15 cm s^{-1}, and 15-20 cm s^{-1} in the upper troposphere at

230 temperatures below -40°C, respectively. During a typical ice nucleation event of 150-300 s, particles with radius of 10 μm can reach heights of 25-50 m below the height where they were nucleated. We assume that particles with radius $<10~\mu$m are too small to leave the air parcel. For completeness, it should be mentioned that we neglect any collision and aggregation process during the initial phase of cirrus formation. Aggregation of ice crystals is another pathway that may lead relatively quickly to particles with radii $>10~\mu$m.

235 ## 3 Simulation results

3.1 Model input from the MOSAiC observations

Meteorological information from MOSAiC radiosondes and aerosol and cirrus retrieval products from combined MOSAiC lidar and radar observations were used as a guide in designing realistic simulation scenarios. Before we start to discuss the essential simulation results in Sect. 3.2 and 3.3, we provide a brief overview of the observed Arctic cirrus and aerosol conditions.

240 The observations were discussed in detail in part 1 (Ansmann et al., 2024a).

Figure 2 shows a complete life cycle of an Arctic cirrus cloud system. According to the cirrus classification in Lynch et al. (2002), all ice cloud systems observed over the central Arctic during the MOSAiC winter half year belong to the synoptic cirrus category. This cirrus type is characterized by ice nucleation cells at cloud top and vertically extended virga zones of falling ice crystals below the generation cells. As can be seen, large scale lofting over 33 hours caused an ascent of the cirrus

245 top layer from about 9.5 km to 11 km height (with a mean lofting velocity of 1.2-1.3 cm s^{-1}). Extended virga reached down to about 4 km above Polarstern (at 87.4°N). The cirrus top temperature and ice saturation ratio were $T = -72$°C and $S_i = 1.36$ at the beginning of the cirrus event (according to the radiosonde launched at 5 UTC on 25 January). Later on the temperatures decreased to -75°C and the ice saturation ratios ranged from 1.25 to 1.32 just below the tropopause.

Figure 3 shows ICNC height profiles (one hour mean profiles of ice crystal number concentrations), derived from combined

250 MOSAiC lidar and radar observations in the cirrus virga zone on 25-26 January 2020. Details are given in part 1 (Ansmann et al., 2024a). In the beginning, high ICNC values up to 100 L^{-1} were observed, later on ICNC decreased to values < 10 L^{-1}. Low ICNC values <50 L^{-1} point to heterogeneous ice nucleation and high ICNC numbers >100 L^{-1} may have been partly caused by homogeneous freezing.
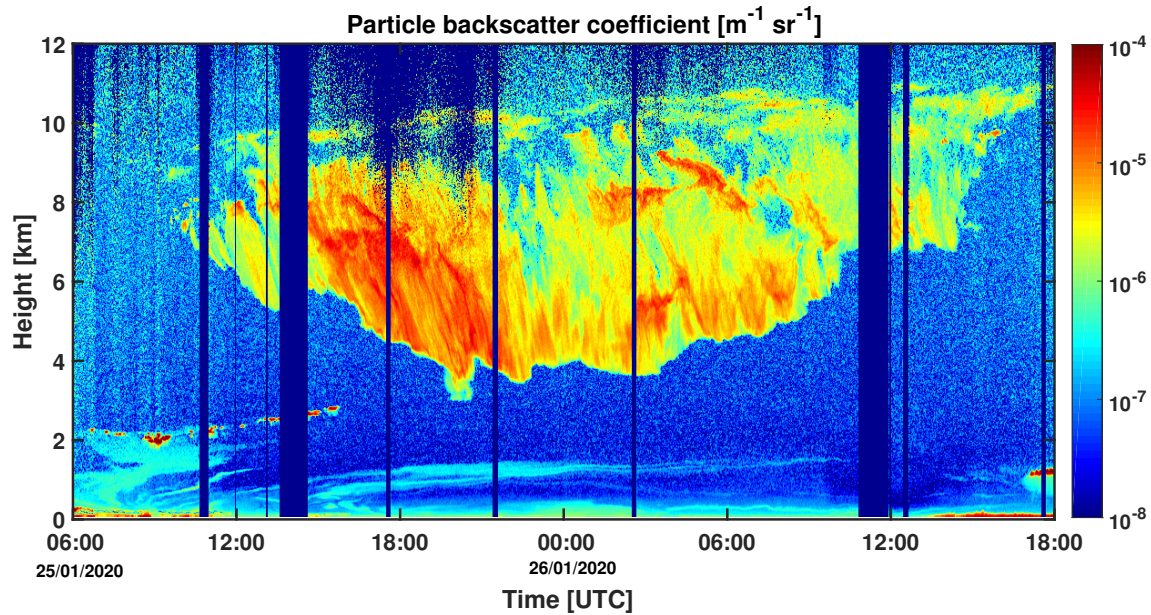
Figure 2. Cirrus life cycle observed with lidar over Polarstern at 87.4°N and 93-94°E on 25-26 January 2020. The cirrus (in light green, yellow and red colors) belongs to the synoptic cirrus category (top down generation of cirrus structures) (Lynch2002). The cirrus top layer (ice nucleation zone) ascended from about 9.8 to 11 km within 33 hours. Ice crystal virga of falling ice crystals developed between 10 and 4 km height. Evaporation of crystals determine the lower rim of the virga zone. The particle backscatter coefficient at 1064 nm is shown. Multiplication of the backscatter coefficients with a cirrus lidar ratio of 30 sr yields the cirrus extinction coefficient.

Unfortunately, observations of cloud radar reflectivity were generally restricted to height regions with comparably large ice
255 crystals so that the uppermost part of the cirrus cloud deck including the ice nucleation zones were not covered by useful radar observations (see part 1). As a consequence, ICNC values could be obtained for the virga zones only, and one must extrapolate the ICNC profiles to the top of the cirrus to estimate the number concentration of freshly nucleated ice crystals. Such an attempt is illustrated in Fig. 3 (see dashed lines). According to the dashed lines we assume that the number concentration of the freshly nucleated crystals was about 4 L^{-1} (blue dashed line) and 300 L^{-1} (red dashed line) at the top of the ice clouds at 10.5 km
260 height.

Fig. 4a provides information about typical ice saturation ratios in the Arctic cirrus layers we investigated during the MOSAiC winter months (Ansmann et al., 2024a). In Fig. 4b, the frequence-of-occurrence distribution of lidar-derived PSAC values observed during the winter months from November to February at the tropopause is given. A typical value of $s_{\mathrm{p}} = 10\ \mu\mathrm{m}^2\ \mathrm{cm}^{-3}$ is considered in the simulations (start value, for $j = 1$). Accordingly, the particle number concentration $n_{250}(j = 1)$ (INP reser-
265 voir) is about 2000 L^{-1} (see Eq. 21). Both panels in Fig. 4 together suggest that aged organic particles are not very efficient INPs. Good INPs such as mineral dust particles would become ice active at 1.05-1.25 (Ullrich et al., 2017; Ansmann et al., 2019; Dekoutsidis et al., 2024) and would probably widely prevent the occurrence of high ice saturation ratios of 1.3-1.4.
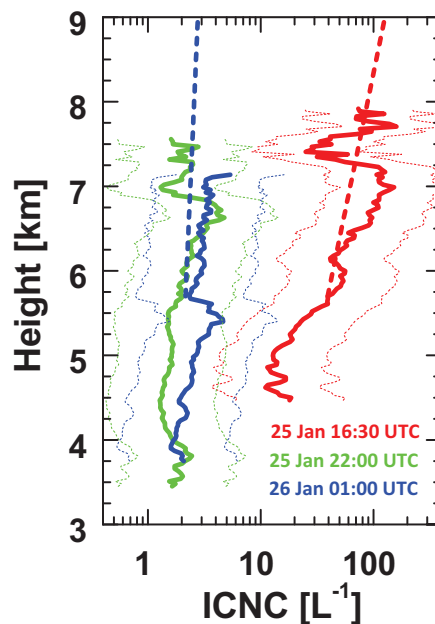
Figure 3. Ice crystal number concentration (ICNC, one hour mean profiles, begin of the measurement period is given in the panel) in ice virga retrieved from combined lidar-radar observations (see part 1 for explanations) on 25-26 January 2020 (see Fig. 2). The thick dashed lines provide a rough estimate of the number concentrations of freshly nucleated ice crystals, when extrapolated to 10.5 km height (cirrus top). ICNC values below $10 \, L^{-1}$ indicate heterogeneous ice nucleation, ICNC $> 100 \, L^{-1}$ may be caused either by heterogeneous ice nucleation on smoke particles or by homogeneous ice nucleation on background sulfate particles. The ICNC retrieval uncertainty range is indicated by thin dashed lines.
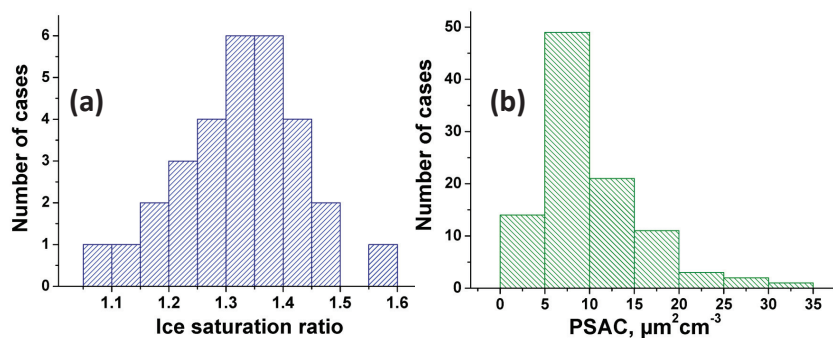
Figure 4. (a) Frequency of occurrence of the maximum or peak ice saturation ratio measured in cirrus layers close to cirrus top. Thirty radiosonde profiles are analyzed (November 2019 to February 2020). (b) Frequency of occurrence of the smoke particle surface area concentration (PSAC) estimated from lidar observations at the tropopause during clear sky conditions (November 2019 to February 2020).

Table 1. Meteorological and aerosol input parameters in the cirrus simulation studies.

Smoke particle surface area concentration	s_{p}	10 $\mu\mathrm{m}^2$ cm^{-3}
Particle volume concentration, background	$v_{\mathrm{p,bg}}$	1.0 $\mu\mathrm{m}^3$ cm^{-3}
INP reservoir	n_{250}	appr. 2000 L^{-1}
Contact angle	c_{angle}	23.5°–26.5°
Starting height (in ascent simulations)	z_0	10.5 km
Temperature at z_0	T	199–218 K
Relative humidity over water at z_0	RH	64%–75%
Ice saturation ratio at z_0	S_{i}	1.2–1.35
Air pressure at z_0	p	212 hPa
Updraft mean vertical velocity	v_{up}	0.1–1.0 m s^{-1}
Water vapor deposition coefficient	α_{i}	0.5
Temporal resolution	Δt	1 s

3.2 Suppression of homogeneous freezing

Before we discuss the simulations of specific MOSAiC cirrus cases, we begin with a few basic simulations to discuss the most important influences and processes active during the onset phase of cirrus formation. Not all of the discussed aspects are relevant for Arctic cirrus, however they should be presented to better classify the specific conditions of cirrus formation in the central Arctic. One of the fundamental questions in cirrus research is: How dominant is homogeneous freezing of the omnipresent background aerosol particles and to what extent heterogeneous ice nucleation on available INPs is able to interfere and to prevent homogeneous freezing (Spichtinger and Gierens, 2009; Spichtinger and Cziczo, 2010; Kärcher et al., 2022)? For the MOSAiC smoke scenario defined in Table 1, Fig. 5 provides an answer in the case of a cold Arctic cirrus with top temperature of about 199 K as observed on 21-22 January 2020 (part 1) (Ansmann et al., 2024a) or on 25-26 January 2020 shown in Fig. 2. A continuously adiabatically rising air parcel (no height limit), ascending with constant vertical velocity of 0.1, 0.2, 0.5, and 1 m s^{-1}, is simulated. The initial ice saturation ratio was set to 1.2 at the starting height $z_0 = 10500$ m. The used contact angle of 26.5° indicates relatively inefficient wildfire smoke INPs.

In the simulation shown in Fig. 5, homogeneous freezing of background aerosol particles needs ice saturation ratios exceeding the onset value of $S_{\mathrm{i,on}} = 1.56$ at 197 K (see blue curve in Fig. 5b). Here and the following, $S_{\mathrm{i,on}}$ is arbitrarily defined by the ice saturation ratio S_{i} for which the ice crystal nucleation rate, $n_{\mathrm{i,hom}}$ or $n_{\mathrm{i,het}}$ for $\Delta t = 1$ s in Eqs. (1) and (2), exceeds the value of 0.001 L^{-1} s^{-1} during a lofting of an air parcel. To reach $S_{\mathrm{i,on}} = 1.56$ in the case of homogeneous freezing the air parcel has to be adiabatically lofted by 191 m. In the case of a low updraft velocity of 0.1 m s^{-1}, more than 30 minutes are required to reach this height. During the ice nucleation phase ($S_{\mathrm{i}} > S_{\mathrm{i,on}}$, 1916-2163 s after the start of the lofting in Fig. 5a) the air parcel ascends from 10691 m to 10716 m height (not shown).
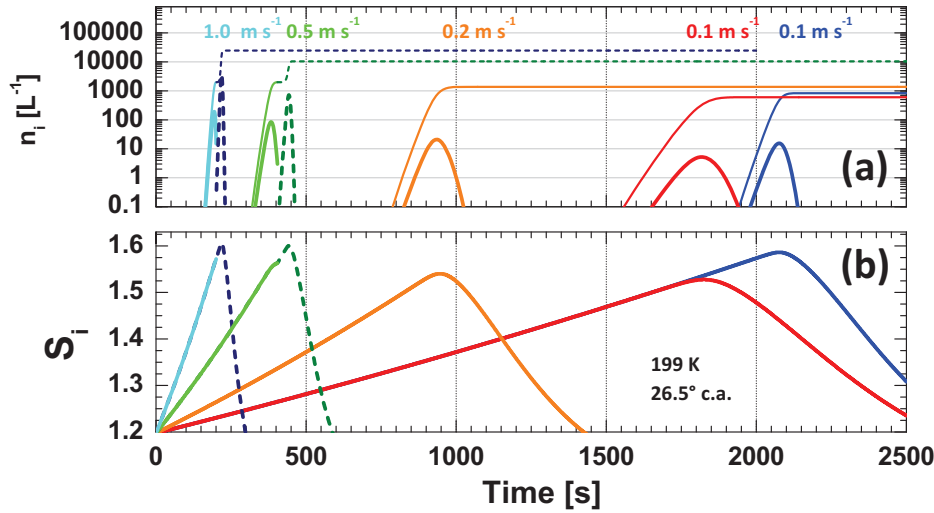
Figure 5. Simulation of heterogeneous ice nucleation on smoke INPs during the adiabatic rise of an air parcel ascending with constant updraft velocity of 0.1 m s^{-1} (red), 0.2 m s^{-1} (orange), 0.5 m s^{-1} (green, solid), and 1.0 m s^{-1} (cyan, solid). In addition, homogeneous freezing of background aerosol particles (blue, updraft velocity of 0.1 m s^{-1}) is shown. Temperature is 199 K and ice saturation ratio is 1.2 at the start of the ascent. (a) Temporal evolution of the ice crystal number concentration $n_i = n_{i,het}$ and $n_i = n_{i,hom}$ (i.e., number of crystals nucleated within $\Delta t = 1$ s), and (b) temporal evolution of the ice saturation ratio S_i. Significant heterogeneous ice nucleation begins when S_i exceeds the onset value of $S_{i,on} = 1.47$ (DIN) and 1.56 (homogeneous freezing). Thick solid lines in (a) show n_i, thin lines the sum $\sum n_i$ of all nucleated crystals. In the case of the 0.5 and 1.0 m s^{-1} updraft simulations, the solid lines stop when the INP reservoir (≈ 2000 L^{-1}) is depleted. Further ascent of the air parcel then leads to ice saturation ratios exceeding the onset $S_{i,on}$ for homogeneous ice nucleation. Dashed olive lines and dashed dark blue lines show $n_{i,hom}$ and $\sum(n_{i,het} + n_{i,hom})$ in (a) and S_i in (b). The strong drop in the S_i values is always caused by ice crystal growth.

The burst-like nucleation period (lasting for more than 4 minutes, thick blue curve in Fig. 5a) is the result of the interplay of two processes (causing opposite effects). The ascent of the air parcel leads to a permanent increase of the ice saturation ratio S_i, and when $S_{i,on}$ is reached, the nucleation event begins. On the other hand, the growth of the freshly formed and already
290   existing ice crystals in the lofted air parcel permanently reduces the water vapor in the air by deposition of water vapor on the ice surfaces. Because of crystal growth the ice saturation ratio S_i decreases according to Eq. (19). As shown in Fig. 5b, when S_i drops below the onset value $S_{i,on}$ again, ice nucleation stops (Fig. 5a). Note that ice growth effect become relevant (strong enough), only, when the number of ice crystals ICNC (or $\sum n_i$) in the air parcel exceed values of around 50 L^{-1}. For ice crystal number concentrations of ICNC < 20 L^{1} growth effects have practically no impact on the ice nucleation rates. In Fig. 5a, the
295   maximum ice nucleation rate exceeds $n_{i,hom} = 10$ L^{-1} s^{-1} (thick blue line) and the number of ice crystals nucleated during the burst (indicated by the thin blue line in Fig. 5a) is $\sum n_i = \sum n_{i,hom} = 832$ L^{-1}.

The simulation of heterogeneous ice nucleation for the scenario with 0.1 m s^{-1} updraft velocity (red curves in Fig. 5a and b) can be directly compared with the homogeneous freezing simulation (for the same 0.1 m s^{-1} updraft scenario). Now, nucleation of ice crystals begins earlier, because $S_\text{i} > S_\text{i,on}$ (=1.47) is already reached 1524 s after the start of the lofting process. The
300   nucleation phase (with $n_\text{i,het} > 0.001 \text{ L}^{-1} \text{ s}^{-1}$) lasts for 480 s. The onset ice saturation ratio $S_\text{i,on}$ is exceeded during the ascent of the air parcel from 10652 m to 10700 m height (not shown). The maximum ice nucleation rate is $n_\text{i,het} = 5.2 \text{ L}^{-1} \text{ s}^{-1}$ (thick red line in Fig. 5a), and the integrated, accumulated number concentration of nucleated ice crystals is $\sum n_\text{i} = \sum n_\text{i,het} = 604 \text{ L}^{-1}$ (see thin red line in Fig. 5a). Again, growth of ice crystals in the lofted air parcel cause the decrease of S_i which begins about 1820 s after the start of the lofting process. Nucleation stops when S_i is again $< S_\text{i,on}$, 2000 s after the start of the
305   lofting process (at 10700 m height).

A similar result is obtained in the case of the scenario with updraft velocities of 0.2 m s^{-1} (orange curves), 0.5 m s^{-1} (green curves), and 1.0 m s^{-1} (cyan curves). $S_\text{i,on}$ is reached after an ascent of around 160 m. The maximum nucleation rate and total number of heterogeneously nucleated ice crystals increases with updraft speed because of the decreasing influence of ice crystal growth effects. With increasing updraft velocity the time period available for the reduction of ice supersaturation by ice
310   crystal growth decreases, and thus the impact on the nucleation rate. The higher updraft velocity, the higher the maximum S_i value and the respective maximum ice nucleation rate $n_\text{i} = n_\text{i,het}$ (thick solid lines in Fig. 5a).

In the simulations with vertical velocities of 0.5 and 1.0 m s^{-1}, the INP reservoir of $n_\text{INP} = n_{250} \approx 2000 \text{ L}^{-1}$ is depleted after an ascent of about 200 m, and after further increase of the ice saturation ratio homogeneous ice nucleation sets in (thick dashed olive and blue lines in Fig. 5a and b). Ice growth cannot prohibit a further increase of S_i when the updraft velocity
315   is so fast. If we would simulate an INP reservoir of 200 L^{-1} or even $\leq 50 \text{ L}^{-1}$ as assumed in the simulations by Kärcher et al. (2022), homogeneous freezing would always dominate, even in the scenarios with 0.1 and 0.2 m s^{-1} updraft velocity. Homogeneous freezing cannot be prevented when the INP reservoir contains 50 L^{-1} or less.

We may conclude from these simulation (with an unlimited lofting height range) that even less efficient INPs such as wildfire smoke particles are able to suppress homogeneous freezing because the onset ice saturation level is lower in the case
320   of heterogeneous ice nucleation than the respective onset value for homogeneous freezing. However, a sufficiently large INP reservoir is required as well and low updraft speeds of $0.1\text{-}0.2 \text{ m s}^{-1}$ so that, as a consequence of strong ice growth effects, the ice saturation ratio S_i can always be kept below the homogeneous freezing onset value $S_\text{i,on}$. The better the INPs, the lower the chance for homogeneous freezing processes, provided the INP reservoir is sufficiently large.

Another point needs to be discussed in this more general simulation part: the impact of crystal sedimentation processes.
325   As mentioned in Sect. 2, we simply assume that all larger ice particles with radius $r_\text{i} > 10 \ \mu\text{m}$ fall out of the air parcel and thus do no longer contribute to ice growth effects in the lofting air parcel. For cold cirrus with top temperatures around 200 K sedimentation effects are not relevant when using this sedimentation parameterization. Ice crystal growth at 200 K is associated with a very slow increase of the crystal size in our simulations. Even 20 minutes after the nucleation onset, the ice particles are not larger than 15-16 μm in diameter (in the simulation with 0.1 m s^{-1} updraft velocity) so that crystal sedimentation processes
330   had no impact on ice growth effects. Note in this context that crystal growth by collision and aggregation processes, that could speed up the growth of crystals, is not considered in our simulations.
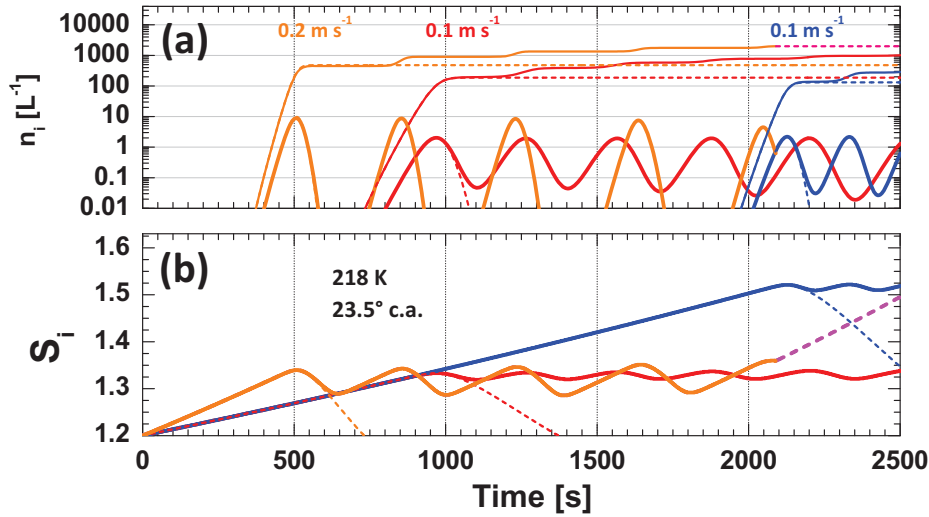
Figure 6. Same as Fig. 5, except for a warm cirrus with top temperature of 218 K and a respectively higher contact angle of 23.5°. In addition, sedimentation effects are now considered. Simulations for the low updraft speed scenarios (0.1 and 0.2 m s^{-1}) are shown only. The strong contrast to Fig. 5, indicated by the oscillating behavior of n_i and S_i, is caused by sedimentation effects (when ice crystals with diameter >20 μm fall out and no longer contribute to ice growth in the simulation). Heterogeneous ice nucleation occurs when S_i exceeds the onset values of $S_{i,on} = 1.31$. The onset value for homogeneous freezing is $S_{i,on} = 1.5$. The thin dashed curves in (a) and (b) are obtained when the sedimentation option is switched off in the simulation. The thick dashed magenta S_i curves (in b, 0.2 m s^{-1} updraft scenario) shows the increase of S_i after depletion of the INP reservoir ($n_{INP} \approx 2000$ L^{-1}).

In contrast to cold cirrus clouds, sedimentation processes have a strong impact on ice nucleation in the case of warm cirrus, i.e., in the case of ice clouds with top temperatures close to 220 K. The reason for the strong difference to cold cirrus clouds is the much higher water vapor molecule number concentration available for the growth of ice crystals in warm cirrus layers.

335 The ice saturation water vapor pressure is 15 times larger at 218 K compared to at 199 K. Crystal growth is fast at 218 K. In an environment with high ice supersaturation of 1.3-1.5, crystals reached diameters of 20 μm in our simulations within less than 200 s after nucleation so that sedimentation effects must be considered in ice growth processes.

Figure 6 shows the results for a warm cirrus scenario with cloud top temperature of 218 K. Note, first of all again, that the efficiency of the smoke particles to serve as DIN INPs increases with temperature as laboratory DIN experiments show (Wang

340 and Knopf, 2011; Wang et al., 2012). This is considered by the decrease of the contact angle from 26.5° at 199 K to 23.5° at 218 K (Wang and Knopf, 2011). The onset ice saturation ratio $S_{i,on}$ decreases from close to 1.5 at 199 K to about 1.25-1.3 at 218 K.

The results in Fig. 6 appear to be unrealistic at a first glance. However, the oscillations in the time series of n_i and S_i can be easily explained. They arise from the fact that after the initial phase with strong ice nucleation, the ice saturation ratio is

345 reduced by crystal growth. More and more crystals then reach the size of 20 μm and fall out of the air parcel. These crystals no

longer contribute to ice growth and to a S_i reduction in our simulation. Further rise of the air parcel then leads to a re-increase of S_i and after exceeding the onset $S_{i,on}$ again another round of ice nucleation takes place followed by strong ice growth and S_i reduction until the sedimentation effect comes into play again. This process repeats several times as long as the air parcel is rising and the INP reservoir is not depleted. The lower the updraft speed the smoother the oscillating structures. By considering

350 sedimentation in the case of warm cirrus the difference between the onset S_i values for heterogeneous ice nucleation and for homogeneous ice nucleation becomes very large and thus homogeneous freezing becomes less likely in warm cirrus clouds as long as the INP reservoir is not depleted. In the case of simulations with stronger updraft speed of 0.5-1 m s^{-1} (not shown) the oscillations are even stronger than in the simulations with 0.2 m s^{-1} updraft velocity.

We can conclude from the simulations with low updraft speeds of 0.1-0.2 m s^{-1} that sedimentation prohibits a rather strong

355 S_i decrease (as given by the orange and red dashed lines in Fig. 6b) and thus cause an increase in the total number of nucleated crystals compared to the respective $\sum n_i$ numbers in the simulations in which the sedimentation impact is switched off. This is shown in Fig. 6a. It should be further mentioned that sedimentation effects are largest in the uppermost nucleation layer of a cirrus system. All other cirrus layers (below this top layer) win and lose crystals by sedimentation processes so that fall out effects are less pronounced in these lower layers.

360 ### 3.3 Gravity wave simulations

Now, we focus on Arctic cirrus. The simulations in the foregoing section showed ICNC levels (or $\sum n_i$) from 100 L^{-1} to more than 1000 L^{-1} instead of 0.1-10 L^{-1} as was mostly observed in the central Arctic during MOSAiC. The main reason is that we simulated ice nucleation in air parcels without any restriction regarding the vertical extent of the updrafts. Obviously the meteorological conditions in the Arctic do not offer such almost unlimited lofting conditions. To obtain a more realistic view

365 on Arctic cirrus formation we move on to simulate gravity-wave-induced adiabatic motions of air parcels (Haag and Kärcher, 2004; Spichtinger et al., 2005; Kalesse and Kollias, 2013; Kärcher and Podglajen, 2019; Barahona et al., 2019; Kärcher et al., 2022).

Kalesse and Kollias (2013) investigated gravity wave dynamics in cirrus layers observed with cloud radar and found typical wave periods of the order of 15-30 minutes. In our simulations, presented next, we selected a gravity wave period of 25 minutes

370 (1500 s) and a vertical velocity of 0.2 m s^{-1} as a typical value for the mean updraft speed during the ascent phase of a gravity wave so that the amplitude A_{GW} of the wave is 75 m (reached 375 s after the start of lofting). With focus on the MOSAiC cirrus events observed on 22 and 25 January 2020, the cirrus top temperature was set to 199 K at 10500 m height and the ice saturation ratio at cirrus top was assumed to be 1.34 at the beginning of the gravity wave simulation. As in the simulations before, we consider the same smoke INP properties and meteorological values at ascent starting height z_0 as given in Table 1.

375 The results are shown in Fig. 7.

As can be seen, now the accumulated number of nucleated crystals is $\sum n_{i,het} = 1.3$ L^{-1} for the nucleation period from about 250 to 500 s after lofting start. Ice nucleation occurs in a rather narrow S_i range from $S_i = 1.47$ to 1.485 at heights from 10568 m to 10575 m, i.e., 68-75 m above the starting height z_0. Ice nucleation rates are $n_{i,het} < 0.012$ L^{-1} s^{-1} (Fig. 7b) at these conditions. Crystal growth and sedimentation effects and assumptions on the INP reservoir do not play any role when the

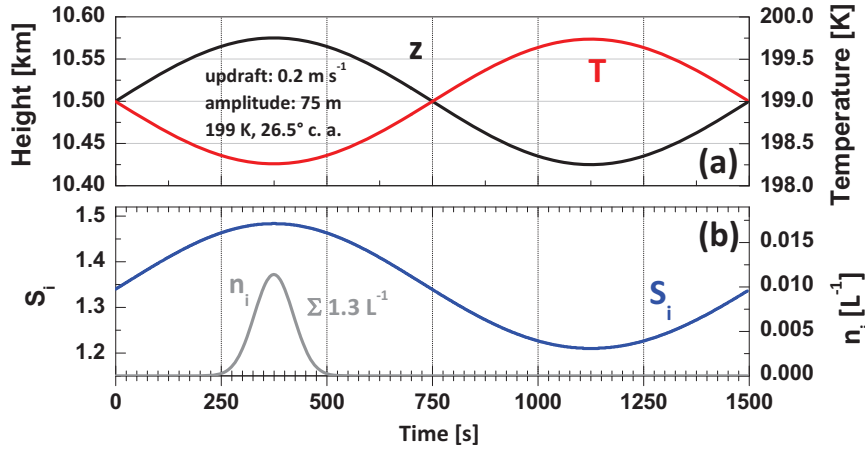**Figure 7.** Heterogeneous ice nucleation during the adiabatic motion (along the black z curve) of a smoke-filled air parcel. The up and downward motion is caused by a gravity wave, characterized by an updraft mean vertical velocity of 0.2 m s^{-1} (during the first quarter of the wave period of 375 s), a wave amplitude of 75 m, temperature T of 199 K at the starting height $z_0 = 10.5$ km (T curve in red in a), and an ice saturation ratio S_i at z_0 of 1.34 (blue curve in b). Significant DIN begins after 275 s ($n_i > 0.001$ L^{-1} s^{-1}, grey curve in b) when the onset ice saturation ratio $S_{i,on} = 1.47$ is exceeded and the nucleation period stops about 200 s later (475 s after the start of the simulation) when S_i drops below $S_{i,on}$ again. The sum $\sum n_{i,het}$ of all heterogeneously nucleated ice crystals is 1.3 L^{-1}. Ice crystal growth is simulated but has no impact when the overall ice crystal number concentration is so low.

380 ICNC values are so low. The amplitude of the gravity wave has a rather sensitive impact on the nucleation rate. In the case of an amplitude of 100 m instead of 75 m, the total number of nucleated crystals $\sum n_{i,het}$ is close to 70 L^{-1}. The impact of the gravity wave amplitude will be further discussed below.

Figure 8 shows the simulation results for a warm cirrus (with top temperature of 218 K at the starting height z_0) with increased ice activity (contact angle of 23.5°) of the organic particles, and an onset ice saturation ratio $S_{i,on}$ of 1.3. S_i was set to

385 1.22 at z_0. For these starting conditions almost 20 ice crystals per liter could be nucleated within the burst-like event lasting for about 250 s (between 250 and 500 s after the start of lofting). Maximum nucleation rates reached almost $n_{i,het} = 0.2$ L^{-1} s^{-1} (Fig. 8b). The cyan S_i curve in Fig. 8b shows the crystal growth effect on S_i. Sedimentation effects weaken the ice-growth-induced decrease of S_i (green curve in Fig. 8b). However, even in the case of this warm cirrus the impact of ice crystal growth on $\sum n_{i,het}$ is low. As mentioned, $\sum n_i > 50$ L^{-1} is required before crystal growth effects influence the ice nucleation rate at

390 a significant level.

Figure 9 provides an overview of the smoke impact on ice formation for the main range of MOSAiC cirrus top temperatures from 199-213 K and different realistic updraft-mean vertical velocities of 0.1, 0.2, and 0.5 m s^{-1}. The simulations were performed for the same wave amplitude of 75 m as used in Figs. 7 and 8. The ice saturation ratio S_i at the starting height z_0 was set to 1.34 (199 K simulations as in Fig. 7) and 1.25 (213 K simulations). Onset values $S_{i,on}$ are 1.47 (199 K scenarios)

395 and 1.35 (213 K scenarios). For these atmospheric conditions, the ICNCs are in the range of 0.1-20 L^{-1} as typically observed
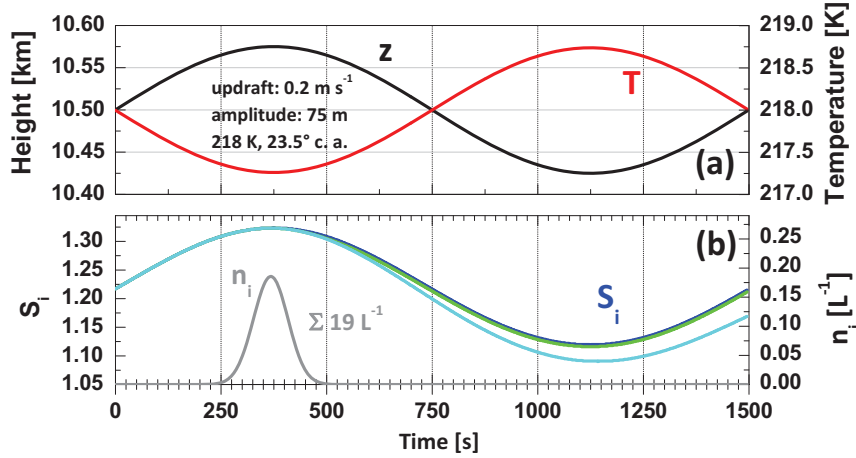
17

Figure 8. Same as Fig. 7, except for a warm cirrus with a temperature of 218 K at starting height z_0, a contact angle of 23.5°, and $S_i = 1.22$ at z_0. The dark blue S_i curve in (b) is obtained when ice growth and sedimentation options are switched off. The cyan S_i curve considers ice growth, but sedimentation remains switched off. The green S_i curve considers even sedimentation effects. As a result of the nucleation event (see gray n_i peak in b), the accumulated number $\sum n_{i,\text{het}}$ of heterogeneously nucleated ice crystals is 19 L^{-1}.

in the MOSAiC cirrus virga. Since the impact of ice crystal growth processes is low for these low ICNCs, the sum of formed ice crystals is a simple function of the time period during which S_i exceeded the onset value $S_{i,\text{on}}$. The stronger the updraft, the shorter the time period with $S_i > S_{i,\text{on}}$ in the simulated air parcel. The maximum S_i values were close to 1.365 (213 K) and 1.485 (199 K) in the simulations when the air parcels reached the maximum height of 75 m above the starting height z_0.

400 The time periods with $S_i > S_{i,\text{on}}$ were about 450 s, 250 s, and 100 s in the simulations with updraft velocities of 0.1, 0.2, and 0.5 m s^{-1}, respectively. The total numbers of nucleated crystals $\sum n_{i,\text{het}}$ were 2.6 L^{-1}, 1.3 L^{-1}, and 0.5 L^{-1} for 199 K and updraft velocities of 0.1, 0.2, and 0.5 m s^{-1}, respectively, and 13 L^{-1}, 8 L^{-1}, and 3.3 L^{-1} in the case of the respective 213 K simulations.

Figure 10 finally shows the impact of the gravity wave amplitude A_{GW} on the accumulated numbers of nucleated ice
405 crystals. As can be seen, the vertical extent of an updraft has a very sensitive impact on ice nucleation. For the simulated range of MOSAiC cirrus top temperatures, contact angles for less efficient INPs (26.5° at 199 K, 24.5° at 213 K) and more efficient smoke INPs (25.0° at 199 K, 23.0° at 213 K) were simulated. Ice supersaturation levels as used in Fig. 9 were chosen. As can be seen, the ICNC values are low (< 50 L^{-1}) as long as the wave amplitudes are < 50 m (for more efficient INPs) and < 90 m (for less efficient INPs). If we use $S_i = 1.25$ at the starting height z_0 also in the 199 K simulations, we need amplitudes of
410 about 100 m (ice-active INPs) to 140 m (less ice-active INPs) before ICNC exceeds values of 50 L^{-1}. The larger the wave amplitude, the longer is the time period available for ice nucleation for a given updraft velocity, the higher the maximum saturation ratio, and thus the sum of nucleated crystals. However, with increasing number of generated ice particles, crystal growth and sedimentation effects come into play so that the finally produced overall crystal numbers remained <1000 L^{-1} in these simulations. In these cases, the INP reservoir would not be depleted.
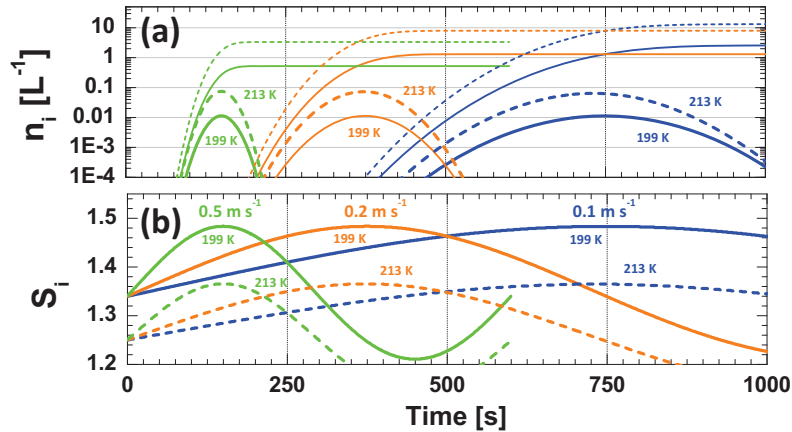
Figure 9. Smoke-related ice nucleation simulations for the main MOSAiC cirrus top temperature range from 199–213 K, a gravity wave amplitude of 75 m, and variable updraft mean vertical velocity of 0.1 m s^{-1} (blue), 0.2 m s^{-1} (orange), and 0.5 m s^{-1} (green). Contact angles are 24.5° (213 K simulations) and 26.5° (199 K simulations). S_i at starting height z_0 is set to 1.25 (213 K simulations) and 1.34 (199 K simulations). The number of ice crystals $n_i = n_{i,het}$, nucleated per second, is plotted as thick lines in (a), the sum $\sum n_i$ is given as thin lines in (a).
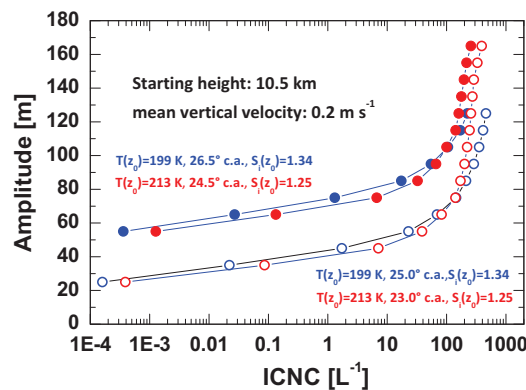
Figure 10. Impact of the gravity wave amplitude on the overall sum of heterogeneously nucleated ice crystals (ICNC) for the main MOSAiC cirrus top temperature range from 199-213 K and a typical updraft-mean vertical velocity of 0.2 m s^{-1}. The start S_i values are 1.34 in the 199 K simulations and 1.25 in the 213 K simulations as in Fig. 9. Different contact angle ranges for a given temperature indicate the sensitive impact of the ice nucleation efficiency of smoke particles on $\sum n_{i,het}$ for a given amplitude.

3.4 Impact of smoke mixtures of very efficient to poor INPs on ice nucleation

The aged wildfire smoke observed over the North Pole region from October 2019 to May 2020 was emitted into the atmosphere over Siberia in July-August 2019. After 3-10 months of long-range transport there may have been many fractions of organic
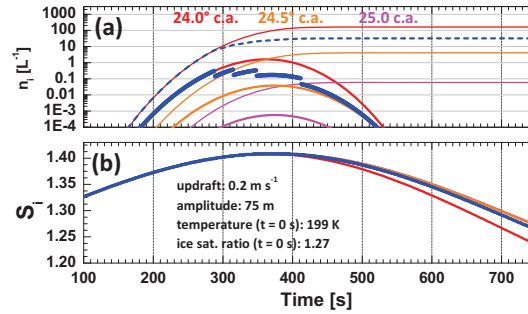
Figure 11. Ice nucleation scenario with a smoke aerosol mixture of efficient to very inefficient INPs characterized by a broad contact angle distribution. $n_i = n_{i,het}$ is given as thick blue line segments, $\sum n_i$ is given as blue dashed line. A Gaussian distribution of contact angles (representing different ice-active smoke particle fractions) is simulated. Cirrus with top temperature is 199 K, the gravity wave amplitude 75 m, and the updraft mean vertical velocity 0.2 m s^{-1}. The corresponding S_i curve is shown in (b) as thick blue line. For comparison the evolution of n_i (thick lines in a), $\sum n_i$ (thin lines in a), and S_i (in b) for scenarios with a single contact angle of 24.0° (red), 24.5° (orange), and 25.0° (magenta) for the entire smoke particle population are shown. In (b), the blue, magenta and orange S_i curves are close together.
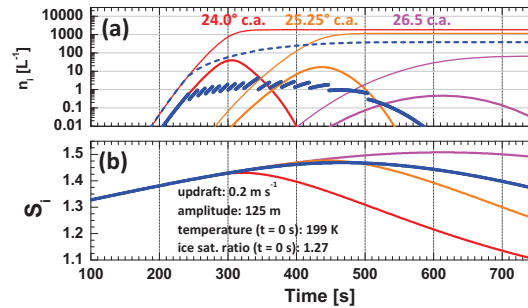
Figure 12. Same as Fig. 11, except for a gravity wave amplitude of 125 m. For comparison, scenarios with a single contact angle of 24.0° (red), 25.25° (orange), and 26.5° (magenta) are simulated.

aerosol particles with very different ice nucleation efficiencies, expressed by contact angles, e.g., from 24° (efficient INPs) to 29° (very inefficient INPs). To provide an impression of the ice activity of a complex aerosol mixture we defined a Gaussian distribution of 50 different smoke INP fractions, characterized by 50 different contact angles from 24° to 29°. The Gaussian distribution was centered at the fraction with a contact angle of 26.5°. The contact angle half width of the Gaussian distribution was 1.25°. The INP reservoir was 2000 L^{-1} as in the previous cases. By using this mixture, we compared the simulation runs with fixed, single contact angle for the entire smoke particle population with the one for the mixture. The results are shown in Figs. 11 and 12. A constant updraft velocity of 0.2 m s^{-1} was simulated. Wave amplitudes were 75 m (Fig. 11) and 125 m (Fig. 12).

In the case of the aerosol mixture, the smoke fraction with the highest ice nucleation efficiency is activated first. When this INP reservoir for the most ice-active fraction (24.0° c.a., 5 INPs) is depleted, the next fraction (24.1° c.a., 7 INPs) becomes

ice-active, and so on. Note again, that the onset saturation ratio $S_{i,on}$ is lowest for 24.0° and increases with increasing contact angle. In the case of a wave amplitude of 75 m, only a few INP fractions become activated (contact angles from 24.0°-24.3°, 32 INPs). The total number $\sum n_{i,het}$ of nucleated crystals is 32, 162, 4, and 0.06 L^{-1} for the contact angle distribution, and the single contact angle simulations of 24.0°, 24.5°, and 25.0°, respectively.

In the case of the wave amplitude of 125 m , more particle fractions, representing different INP reservoirs, become activated (contact angles now from 24.0°-25.6°). As a consequence, the ice nucleation phase (defined by $S_i > S_{i,on}$) is long with about 427 s. For comparison, the nucleation periods are 212s and 276s in the case of the simulations with the contact angles of 24.0° and 25.25°, respectively. The total number $\sum n_{i,het}$ of nucleated crystals is 384 L^{-1} for the aerosol mixture, and 1841, 1154, and 67 L^{-1}, respectively, in the case of the simulations with the single contact angles of 24.0°, 25.25°, and 26.5°, respectively.

3.5 Discussion: summary of main observational and modeling findings

The simulation of an air parcel rising with constant updraft velocity demonstrated that nucleation of ice crystals during the period with $S_i > S_{i,on}$ and the growth of the nucleated ice particles are the main processes that control the ice nucleation rate at conditions with large vertical extension (> 150 m) of the updraft zones. ICNC mainly ranged from a few 100 to a few 1000 crystals per liter in these basic simulations. However, such "unlimited" ascent conditions (with air parcel lofting over 200 m and more) are not typical in the central Arctic. Furthermore, these simulations indicate that to prevent homogeneous freezing, a large reservoir of potential DIN INPs was needed.

In the next step, in our simulations we considered realistic gravity wave characteristics in addition to the enhanced wildfire smoke pollution levels. By assuming ice saturation ratios and cirrus temperatures, as measured with radiosondes during the MOSAiC expeditions, the ICNC values dropped to numbers below 50 L^{-1} in the case of shallow gravity waves with amplitudes $A_{GW} < 100$ m. For the conditions of low ICNC, ice growth effects in the rising air parcels are no longer relevant. The crystal nucleation rate is then mainly a function of the time period during ascent with $S_i > S_{i,on}$.

By combining of the simulation results in this part 2 with the observations, presented in part 1 (Ansmann et al., 2024a), we can now discuss the potential impact of smoke particles in a more consistent and holistic/comprehensive way. The lidar-radar observations revealed in most of the analyzed cirrus events low ice crystal number concentrations of 0.1-10 L^{-1} in the cirrus virga. This finding points to the dominance of heterogeneous ice nucleation. The radiosonde observation showed frequently high ice saturation ratios of 1.3-1.4 in the upper part of cirrus clouds in the presence of elevated levels of wildfire smoke pollution characterized by PSAC of 5–15 μm^2 cm^{-3}. The high supersaturation values exclude a major role of very ice-active INPs such as mineral dust particles. The high ice saturation ratios point to heterogeneous ice formation on less efficient INPs, as expected in the case of aged organic particles.

In part 2, we performed simulations for realistic gravity waves (period, updraft velocity, amplitude), typical MOSAiC cirrus top temperatures of 199-213 K, and observed ice supersaturation levels. For these carefully selected scenarios, we found low ICNCs as long as the amplitudes of the gravity waves were small (≤ 100 m) and updraft speeds were of the order of 0.1-0.5 m s^{-1}, which appear to be reasonable properties of gravity waves at high northern latitudes close to the North Pole. Such low ICNCs also indicate that the number of activated INPs was too low to deplete the INP reservoir. This is in agreement

with the MOSAiC observations in part 1. A significant decrease of the wildfire pollution levels was not found from December 2019 to March 2020 although we observed many ice clouds including many long-lasting cirrus events (partly continuously observable over 4-6 days). It is worthwhile to add that our multiwavelength Raman polarization lidar observations (Ohneiser et al., 2021) clearly point to the dominance of wildfire smoke at cirrus height levels. However, a very small impact of meteoritic particles, mineral dust particles, or fine-mode volcanic ash particles coated with sulfate on DIN cannot be excluded.

We can further conclude: In the case of a clean upper troposphere with background particles (or with a very small INP reservoir that can quickly be depleted), gravity wave amplitudes of > 200 m are needed to initiate homogeneous freezing of background aerosol particles. Such strong and vertically extended updrafts do not frequently occur. Since ice nucleation can be initiated in much weaker updrafts with amplitudes from 70 to 100 m in the presence of even less efficient INPs, cirrus can form more frequently than in a clean upper troposphere because weaker updrafts and lower amplitudes occur most probably much more frequently than updrafts in a gravity wave with a 200 m vertical extent. This hypothesis is in consistency with the finding that 30% of all observations with the continuously running MOSAiC lidar showed cirrus signatures. A minimum cirrus frequency of occurrence of 10% was expected (Sassen et al., 2008, 2009).

4 Conclusions and outlook

We investigated the potential impact of heterogeneous ice nucleation on wildfire smoke particles on Arctic cirrus formation processes described in part 1 and part 2 (this article). We combined state-of-the-art active remote sensing of Arctic ice clouds with lidar and radar instruments aboard the ice breaker Polarstern at latitudes $> 85°$N with complex cirrus modeling. In part 1, we analyzed the MOSAiC lidar, radar, and radiosonde observations, performed at latitudes $> 85°$N during the winter halfyear from October 2919 to March 2020. As discussed in the foregoing Sect. 3.5, we found a number of strong indications and arguments that heterogeneous ice nucleation initiated by Siberian wildfire smoke particles serving as INPs dominated cirrus formation in the central Arctic during the winter halfyear 2019-2020.

In part 2, we discussed the results of cirrus simulations, performed with the goal to gain a deeper insight into cirrus evolution as a function of the observed environmental and meteorological conditions (temperature, relative humidity) and by considering realistic gravity wave characteristics (updraft speed, wave amplitude). The simulations were found to be in line with the observations and strongly support that the smoke INPs were able to trigger ice nucleation in the presence of high ice saturation ratios of 1.3–1.5 over the North Pole region at cirrus top temperatures mostly $< -60°$C.

However, disregarding the numerous arguments for a significant smoke impact on ice formation in the Arctic upper troposphere, a caveat of our study is that we do not know the exact deposition ice nucleation properties of wildfire smoke particles that aged over months of long range transport in the upper troposphere and lower stratosphere. INP-related laboratory studies for this special particle type are not available. We applied a deposition ice nucleation parameterization that reflects characteristics of organic particles derived from laboratory studies (Wang and Knopf, 2011; Wang et al., 2012). These organic surrogate INP particles possess a highly viscous including solid, phase state and oxygenated functional groups as would be expected for actual UTLS smoke particles (Knopf et al., 2018). It is unlikely that the ice nucleation efficiency of an organic smoke particle

495 would be orders of magnitude different as studies on organic particles serving as INPs have shown (Murray et al., 2010; Knopf et al., 2018; Wolf et al., 2020). Clearly, more research including the collection of smoke particles and laboratory studies (e.g. Knopf et al., 2023b) and airborne in situ measurements (Cziczo et al., 2017) are required in this exciting field of atmospheric research.

In this context, it should be added that the observed aerosol in the upper troposphere during the MOSAiC winter 2019 and
500 2020 was definitely not dominated by volcanic sulfate aerosol (Ohneiser et al., 2021; Ansmann et al., 2024b), as Boone et al. (2022) and Boone (2024) claim. Liquid volcanic sulfate particles would exclusively contribute to homogeneous freezing and thus would lead to high ICNC numbers, clearly above 100-200 L^{-1}. During MOSAiC we found the opposite, very low ICNCs most of the time, as expected in the case of heterogeneous ice nucleation on smoke INPs.

As an outlook, we plan to extend our smoke-cirrus interaction studies. In the framework of the DACAPO-PESO (Dynamics,
505 Aerosol, Cloud and Precipitation Observations in the Pristine Environment of the Southern Ocean) campaign in Punta Areans, southern Chile (Radenz et al., 2021), we continuously monitored smoke layers in the upper troposphere and the stratosphere in 2020 and 2021 originating from the record-breaking bushfires in eastern Australia in December 2019 and January 2020 (Ohneiser et al., 2020, 2022). Many cirrus layers developed in the polluted upper troposphere over the southernmost tip of South America, in the usually rather clean atmosphere over the Southern Ocean. A unique lidar-radar data set is thus available
510 to explore the impact of the Australian smoke (from burning of eucalyptus trees) on midlatitude cirrus formation in the usually very clean southern hemisphere.

5 Data availability

Polly lidar observations (level 0 data, measured signals) are in the PollyNet database (Polly, 2024). All the analysis products are available at TROPOS upon request (polly@tropos.de) and at https://doi.pangaea.de/10.1594/PANGAEA.935539 (Ohneiser
515 et al., 2021). Cloud radar data are downloaded from the ARM data base (ARM, 2024; ARM-MOSAiC, 2024). MOSAiC radiosonde data are available at https://doi.org/10.1594/PANGAEA.928656 (Maturilli et al., 2021, 2022). Products from synergistic lidar-radar studies and cirrus simulation results can be obtained on request (by contacting the corresponding author).

6 Author contributions

The paper was written and designed by AA and DAK, data analysis was performed by CJ, JR, JB, KO, and RE. AA developed
520 the simulation model and produced the simulation results. All coauthors were actively involved in the extended discussions and the elaboration of the final design of the manuscript.

7 Competing interests

Daniel A. Knopf is a member of the editorial board of Atmospheric Chemistry and Physics

8 Financial support

540 **References**

Ansmann, A., Mamouri, R.-E., Bühl, J., Seifert, P., Engelmann, R., Hofer, J., Nisantzi, A., Atkinson, J. D., Kanji, Z. A., Sierau, B., Vrekoussis, M., and Sciare, J.: Ice-nucleating particle versus ice crystal number concentration in altocumulus and cirrus layers embedded in Saharan dust: a closure study, Atmospheric Chemistry and Physics, 19, 15 087–15 115, https://doi.org/10.5194/acp-19-15087-2019, 2019.

Ansmann, A., Ohneiser, K., Mamouri, R.-E., Knopf, D. A., Veselovskii, I., Baars, H., Engelmann, R., Foth, A., Jimenez, C., Seifert, P., and
545   Barja, B.: Tropospheric and stratospheric wildfire smoke profiling with lidar: mass, surface area, CCN, and INP retrieval, Atmospheric Chemistry and Physics, 21, https://doi.org/10.5194/acp-21-9779-2021, 2021.

Ansmann, A., Ohneiser, K., Engelmann, R., Radenz, M., Griesche, H., Hofer, J., Althausen, D., Creamean, J. M., Boyer, M. C., Knopf, D. A., Dahlke, S., Maturilli, M., Gebauer, H., Bühl, J., Jimenez, C., Seifert, P., and Wandinger, U.: Annual cycle of aerosol properties over the central Arctic during MOSAiC 2019–2020 – light-extinction, CCN, and INP levels from the boundary layer to the tropopause,
550   Atmospheric Chemistry and Physics, 23, 12 821–12 849, https://doi.org/10.5194/acp-23-12821-2023, 2023.

Ansmann, A., Jimenez, C., Roschke, J., Bühl, J., Ohneiser, K., Engelmann, R., Radenz, M., Griesche, H., Hofer, J., Althausen, D., Knopf, D. A., Dahlke, S., Maturilli, M., Gaudek, T., Seifert, P., and Wandinger, U.: Impact of wildfire smoke on Arctic cirrus formation, part 1: observations during MOSAiC 2019-2020, EGUsphere, 2024, 1–YYY, https://doi.org/10.5194/egusphere-2024-XXXX, 2024a.

Ansmann, A., Veselovskii, I., Ohneiser, K., and Chudnovsky, A.: Comment on "Stratospheric Aerosol Composition Observed by the Atmo-
555   spheric Chemistry Experiment Following the 2019 Raikoke Eruption" by Boone et al., Journal of Geophysical Research: Atmospheres, 129, e2022JD038 080, https://doi.org/https://doi.org/10.1029/2022JD038080, e2022JD038080 2022JD038080, 2024b.

ARM-MOSAiC(2024): Atmospheric Radiation Measurement (ARM) user facility, 2019, updated hourly, Ka ARM Zenith Radar (KAZR-CFRGE), 2019-10-11 to 2020-09-20, ARM Mobile Facility (MOS) MOSAIC (Drifting Obs - Study of Arctic Climate), AMF2 (M1), compiled by I. Lindenmaier, D. Nelson, B. Isom, J. Hardin, A. Matthews, T. Wendler, and V. Castro, ARM Data Center, last access: 13
560   February, 2024.

ARM(2024): Atmospheric Radiation Measurement (ARM) user facility, data are collected through routine operations and scientific field experiments, US Department of Energy (DOE), available at https://arm.gov/data, last access: 22 January 2024, 2024.

Barahona, D., Molod, A., and Kalesse, H.: Direct estimation of the global distribution of vertical velocity within cirrus clouds, Sci. Rep., 7, https://doi.org/10.1038/s41598-017-07038-6, 2019.

565 Boone, C. D.: Reply to: "Comment on 'Stratospheric Aerosol Composition Observed by the Atmospheric Chemistry Experiment Following the 2019 Raikoke Eruption' by Boone et al." by Ansmann et al., Journal of Geophysical Research: Atmospheres, 129, e2023JD039 755, https://doi.org/https://doi.org/10.1029/2023JD039755, e2023JD039755 2023JD039755, 2024.

Boone, C. D., Bernath, P. F., Labelle, K., and Crouse, J.: Stratospheric Aerosol Composition Observed by the Atmospheric Chemistry Experiment Following the 2019 Raikoke Eruption, Journal of Geophysical Research: Atmospheres, 127, e2022JD036 600,
570   https://doi.org/https://doi.org/10.1029/2022JD036600, e2022JD036600 2022JD036600, 2022.

Cziczo, D. J., Ladino, L., Boose, Y., Kanji, Z. A., Kupiszewski, P., Lance, S., Mertes, S., and Wex, H.: Measurements of Ice Nucleating Particles and Ice Residuals, Meteorological Monographs, 58, 8.1 – 8.13, https://doi.org/10.1175/AMSMONOGRAPHS-D-16-0008.1, 2017.

Dekoutsidis, G., Wirth, M., and Groß, S.: The effects of warm-air intrusions in the high Arctic on cirrus clouds, Atmospheric Chemistry and
575   Physics, 24, 5971–5987, https://doi.org/10.5194/acp-24-5971-2024, 2024.

DeMott, P. J., Prenni, A. J., Liu, X., Kreidenweis, S. M., Petters, M. D., Twohy, C. H., Richardson, M. S., Eidhammer, T., and Rogers, D. C.: Predicting global atmospheric ice nuclei distributions and their impacts on climate, Proc. Natl. Acad. Sci. USA, 107, 11 217–11 222, https://doi.org/10.1073/pnas.0910818107, 2010.

Haag, W. and Kärcher, B.: The impact of aerosols and gravity waves on cirrus clouds at midlatitudes, Journal of Geophysical Research: Atmospheres, 109, https://doi.org/10.1029/2004JD004579, 2004.

Heymsfield, A. J., Krämer, M., Luebke, A., Brown, P., Cziczo, D. J., Franklin, C., Lawson, P., Lohmann, U., McFarquhar, G., Ulanowski, Z., and Tricht, K. V.: Cirrus Clouds, Meteorological Monographs, 58, 2.1 – 2.26, https://doi.org/10.1175/AMSMONOGRAPHS-D-16-0010.1, 2017.

Kalesse, H. and Kollias, P.: Climatology of high cloud dynamics using profiling ARM Doppler radar observations, Journal of Climate, 26, 6340–6359, https://doi.org/10.1175/JCLI-D-12-00695.1, 2013.

Kanji, Z. A., Florea, O., and Abbatt, J. P. D.: Ice formation via deposition nucleation on mineral dust and organics: dependence of onset relative humidity on total particulate surface area, Environmental Research Letters, 3, 025 004, https://doi.org/10.1088/1748-9326/3/2/025004, 2008.

Khvorostyanov, V. I. and Curry, J. A.: Fall Velocities of Hydrometeors in the Atmosphere: Refinements to a Continuous Analytical Power Law, Journal of the Atmospheric Sciences, 62, 4343 – 4357, https://doi.org/10.1175/JAS3622.1, 2005.

Knopf, D. A. and Alpert, P. A.: A water activity based model of heterogeneous ice nucleation kinetics for freezing of water and aqueous solution droplets, Farad. Discuss., 165, 513–534, https://doi.org/10.1039/c3fd00035d, 2013.

Knopf, D. A. and Alpert, P. A.: Atmospheric ice nucleation, Nature Reviews Physics, 5, 203–217, https://doi.org/10.1038/s42254-023-00570-7, 2023.

Knopf, D. A. and Rigg, Y. J.: Homogeneous Ice Nucleation From Aqueous Inorganic/Organic Particles Representative of Biomass Burning: Water Activity, Freezing Temperatures, Nucleation Rates, The Journal of Physical Chemistry A, 115, 762–773, https://doi.org/10.1021/jp109171g, pMID: 21235213, 2011.

Knopf, D. A., Alpert, P. A., and Wang, B.: The role of organic aerosol in atmospheric ice nucleation: a review, ACS Earth and Space Chemistry, 2, 168–202, https://doi.org/10.1021/acsearthspacechem.7b00120, 2018.

Knopf, D. A., Silber, I., Riemer, N., Fridlind, A. M., and Ackerman, A. S.: A 1D Model for Nucleation of Ice From Aerosol Particles: An Application to a Mixed-Phase Arctic Stratus Cloud Layer, Journal of Advances in Modeling Earth Systems, 15, e2023MS003 663, https://doi.org/10.1029/2023MS003663, e2023MS003663 2023MS003663, 2023a.

Knopf, D. A., Wang, P., Wong, B., Tomlin, J. M., Veghte, D. P., Lata, N. N., China, S., Laskin, A., Moffet, R. C., Aller, J. Y., Marcus, M. A., and Wang, J.: Physicochemical characterization of free troposphere and marine boundary layer ice-nucleating particles collected by aircraft in the eastern North Atlantic, Atmospheric Chemistry and Physics, 23, 8659–8681, https://doi.org/10.5194/acp-23-8659-2023, 2023b.

Koop, T. and Zobrist, B.: Parameterizations for ice nucleation in biological and atmospheric systems, Phys. Chem. Chem. Phys., 11, 10 839–10 850, https://doi.org/10.1039/B914289D, 2009.

Koop, T., Luo, B. P., Tsias, A., and Peter, T.: Water activity as the determinant for homogeneous ice nucleation in aqueous solutions, Nature, 406, 611–614, https://doi.org/10.1038/35020537, 2000.

Kärcher, B. and Podglajen, A.: A Stochastic Representation of Temperature Fluctuations Induced by Mesoscale Gravity Waves, Journal of Geophysical Research: Atmospheres, 124, 11 506–11 529, https://doi.org/10.1029/2019JD030680, 2019.

Kärcher, B., DeMott, P. J., Jensen, E. J., and Harrington, J. Y.: Studies on the Competition Between Homogeneous and
Heterogeneous Ice Nucleation in Cirrus Formation, Journal of Geophysical Research: Atmospheres, 127, e2021JD035 805,
615   https://doi.org/10.1029/2021JD035805, e2021JD035805 2021JD035805, 2022.

Kärcher, B., Jensen, E. J., Pokrifka, G. F., and Harrington, J. Y.: Ice Supersaturation Variability in Cirrus Clouds: Role
of Vertical Wind Speeds and Deposition Coefficients, Journal of Geophysical Research: Atmospheres, 128, e2023JD039 324,
https://doi.org/10.1029/2023JD039324, e2023JD039324 2023JD039324, 2023.

Lohmann, U., Lüönd, F., and Mahrt, F.: An Introduction to Clouds: From the Microscale to Climate, Cambridge University Press,
620   https://doi.org/10.1017/CBO9781139087513, 2016.

Lynch, D. K., Sassen, K., Starr, D. O., and Stephens, G.: Cirrus, Oxford University Press,
https://doi.org/10.1093/oso/9780195130720.003.0019, 2002.

Maturilli, M., Holdridge, D. J., Dahlke, S., Graeser, J., Sommerfeld, A., Jaiser, R., Deckelmann, H., and Schulz, A.: Initial radiosonde data
from 2019-10 to 2020-09 during project MOSAiC, https://doi.org/10.1594/PANGAEA.928656, 2021.

625 Maturilli, M., Sommer, M., Holdridge, D. J., Dahlke, S., Graeser, J., Sommerfeld, A., Jaiser, R., Deckelmann, H., and Schulz, A.: MOSAiC
radiosonde data (level 3) [dataset publication series], https://doi.org/10.1594/PANGAEA.943870, 2022.

Murray, B. J., Wilson, T. W., Dobbie, S., and Cui, Z.: Heterogeneous nucleation of ice particles on glassy aerosols under cirrus conditions,
Nature Geoscience, 3, 233–237, https://doi.org/10.1038/ngeo817, 2010.

Nixdorf, U., Dethloff, K., Rex, M., Shupe, M., Sommerfeld, A., Perovich, D., Nicolaus, M., Heuze´, C., Rabe, B., Loose, B., Damm, E.,
630   Gradinger, R., Fong., A, Maslowski, W., Rinke, A., Kwok, R., Spreen, G., Wendisch, M., Herber, A., Hirsekorn, M., Mohaupt, V., Frick-
enhaus, S., Immerz, A., Weiss-Tuider, K., König, B., Mengedoht, D., Regnery, J., Gerchow, P., Ransby, D., Krumpen, T., Morgenstern,
A., Haas, C., Kanzow, T., Rack, F. R., Saitzev, V., Sokolov, V., Makarov, A., Schwarze, S., Wunderlich, T., Wurr, K., and Boetius, A.:
MOSAiC extended acknowledgement, Zenodo, https://doi.org/10.5281/zenodo.5179738, 2021.

Ohneiser, K., Ansmann, A., Baars, H., Seifert, P., Barja, B., Jimenez, C., Radenz, M., Teisseire, A., Floutsi, A., Haarig, M., Foth, A.,
635   Chudnovsky, A., Engelmann, R., Zamorano, F., Bühl, J., and Wandinger, U.: Smoke of extreme Australian bushfires observed in the
stratosphere over Punta Arenas, Chile, in January 2020: optical thickness, lidar ratios, and depolarization ratios at 355 and 532 nm,
Atmospheric Chemistry and Physics, 20, 8003–8015, https://doi.org/10.5194/acp-20-8003-2020, 2020.

Ohneiser, K., Ansmann, A., Chudnovsky, A., Engelmann, R., Ritter, C., Veselovskii, I., Baars, H., Gebauer, H., Griesche, H., Radenz, M.,
Hofer, J., Althausen, D., Dahlke, S., and Maturilli, M.: The unexpected smoke layer in the High Arctic winter stratosphere during MOSAiC
640   2019–2020, Atmospheric Chemistry and Physics, 21, 15 783–15 808, https://doi.org/10.5194/acp-21-15783-2021, 2021.

Ohneiser, K., Ansmann, A., Kaifler, B., Chudnovsky, A., Barja, B., Knopf, D. A., Kaifler, N., Baars, H., Seifert, P., Villanueva, D., Jimenez,
C., Radenz, M., Engelmann, R., Veselovskii, I., and Zamorano, F.: Australian wildfire smoke in the stratosphere: the decay phase in
2020/21 and impact on ozone depletion, Atmospheric Chemistry and Physics Discussions, 2022, 1–41, https://doi.org/10.5194/acp-2021-
1097, 2022.

645 Polly(2024): PollyNET lidar data base, available at: http://polly.tropos.de/, last access: 10 January, 2024.

Radenz, M., Bühl, J., Seifert, P., Baars, H., Engelmann, R., Barja González, B., Mamouri, R.-E., Zamorano, F., and Ansmann, A.: Hemi-
spheric contrasts in ice formation in stratiform mixed-phase clouds: disentangling the role of aerosol and dynamics with ground-based
remote sensing, Atmospheric Chemistry and Physics, 21, 17 969–17 994, https://doi.org/10.5194/acp-21-17969-2021, 2021.

Riechers, B., Wittbracht, F., Hütten, A., and Koop, T.: The homogeneous ice nucleation rate of water droplets produced in a microfluidic
650   device and the role of temperature uncertainty, Phys. Chem. Chem. Phys., 15, 5873–5887, https://doi.org/10.1039/C3CP42437E, 2013.

Rigg, Y. J., Alpert, P. A., and Knopf, D. A.: Immersion freezing of water and aqueous ammonium sulfate droplets initiated by humic-like substances as a function of water activity, Atmospheric Chemistry and Physics, 13, 6603–6622, https://doi.org/10.5194/acp-13-6603-2013, 2013.

Sassen, K., Wang, Z., and Liu, D.: Global distribution of cirrus clouds from CloudSat/Cloud-Aerosol Lidar and Infrared Pathfinder Satellite Observations (CALIPSO) measurements, Journal of Geophysical Research: Atmospheres, 113, https://doi.org/10.1029/2008JD009972, 2008.

Sassen, K., Wang, Z., and Liu, D.: Cirrus clouds and deep convection in the tropics: Insights from CALIPSO and CloudSat, Journal of Geophysical Research: Atmospheres, 114, https://doi.org/10.1029/2009JD011916, 2009.

Schneider, J., Höhler, K., Wagner, R., Saathoff, H., Schnaiter, M., Schorr, T., Steinke, I., Benz, S., Baumgartner, M., Rolf, C., Krämer, M., Leisner, T., and Möhler, O.: High homogeneous freezing onsets of sulfuric acid aerosol at cirrus temperatures, Atmospheric Chemistry and Physics, 21, 14 403–14 425, https://doi.org/10.5194/acp-21-14403-2021, 2021.

Schröder, F., Kärcher, B., Fiebig, M., and Petzold, A.: Aerosol states in the free troposphere at northern midlatitudes, Journal of Geophysical Research: Atmospheres, 107, LAC 8–1–LAC 8–8, https://doi.org/10.1029/2000JD000194, 2002.

Shupe, M. D., Rex, M., Blomquist, B., Ola, P., Persson, G., Schmale, J., Uttal, T., Althausen, D., Angot, H., Archer, S., Bariteau, L., Beck, I., Bilberry, J., Bucci, S., Buck, C., Boyer, M., Brasseur, Z., Brooks, I. M., Calmer, R., Cassano, J., Castro, V., Chu, D., Costa, D., Cox, C. J., Creamean, J., Crewell, S., Dahlke, S., Damm, E., de Boer, G., Deckelmann, H., Dethloff, K., Dütsch, M., Ebell, K., Ehrlich, A., Ellis, J., Engelmann, R., Fong, A. A., Frey, M. M., Gallagher, M. R., Ganzeveld, L., Gradinger, R., Graeser, J., Greenamyer, V., Griesche, H., Griffiths, S., Hamilton, J., Heinemann, G., Helmig, D., Herber, A., Heuzé, C., Hofer, J., Houchens, T., Howard, D., Inoue, J., Jacobi, H.-W., Jaiser, R., Jokinen, T., Jourdan, O., Jozef, G., King, W., Kirchgaessner, A., Klingebiel, M., Krassovski, M., Krumpen, T., Lampert, A., Landing, W., Laurila, T., Lawrence, D., Lonardi, M., Loose, B., Lüpkes, C., Maahn, M., Macke, A., Maslowski, W., Marsay, C., Maturilli, M., Mech, M., Morris, S., Moser, M., Nicolaus, M., Ortega, P., Osborn, J., Pätzold, F., Perovich, D. K., Petäjä, T., Pilz, C., Pirazzini, R., Posman, K., Powers, H., Pratt, K. A., Preußer, A., Quéléver, L., Radenz, M., Rabe, B., Rinke, A., Sachs, T., Schulz, A., Siebert, H., Silva, T., Solomon, A., Sommerfeld, A., Spreen, G., Stephens, M., Stohl, A., Svensson, G., Uin, J., Viegas, J., Voigt, C., von der Gathen, P., Wehner, B., Welker, J. M., Wendisch, M., Werner, M., Xie, Z., and Yue, F.: Overview of the MOSAiC expedition: Atmosphere, Elementa: Science of the Anthropocene, 10, https://doi.org/10.1525/elementa.2021.00060, 2022.

Skrotzki, J., Connolly, P., Schnaiter, M., Saathoff, H., Möhler, O., Wagner, R., Niemand, M., Ebert, V., and Leisner, T.: The accommodation coefficient of water molecules on ice – cirrus cloud studies at the AIDA simulation chamber, Atmospheric Chemistry and Physics, 13, 4451–4466, https://doi.org/10.5194/acp-13-4451-2013, 2013.

Spichtinger, P. and Cziczo, D. J.: Impact of heterogeneous ice nuclei on homogeneous freezing events in cirrus clouds, Journal of Geophysical Research: Atmospheres, 115, https://doi.org/https://doi.org/10.1029/2009JD012168, 2010.

Spichtinger, P. and Gierens, K. M.: Modelling of cirrus clouds – Part 1a: Model description and validation, Atmospheric Chemistry and Physics, 9, 685–706, https://doi.org/10.5194/acp-9-685-2009, 2009.

Spichtinger, P., Gierens, K., and Dörnbrack, A.: Formation of ice supersaturation by mesoscale gravity waves, Atmospheric Chemistry and Physics, 5, 1243–1255, https://doi.org/10.5194/acp-5-1243-2005, 2005.

Spichtinger, P., Marschalik, P., and Baumgartner, M.: Impact of formulations of the homogeneous nucleation rate on ice nucleation events in cirrus, Atmospheric Chemistry and Physics, 23, 2035–2060, https://doi.org/10.5194/acp-23-2035-2023, 2023.

Ullrich, R., Hoose, C., Möhler, O., Niemand, M., Wagner, R., Höhler, K., Hiranuma, N., Saathoff, H., and Leisner, T.: A New Ice Nucleation Active Site Parameterization for Desert Dust and Soot, Journal of the Atmospheric Sciences, 74, 699–717, https://doi.org/10.1175/JAS-D-16-0074.1, 2017.

690 Wang, B. and Knopf, D. A.: Heterogeneous ice nucleation on particles composed of humic-like substances impacted by O_3, Journal of Geophysical Research: Atmospheres, 116, https://doi.org/10.1029/2010JD014964, 2011.

Wang, B., Lambe, A. T., Massoli, P., Onasch, T. B., Davidovits, P., Worsnop, D. R., and Knopf, D. A.: The deposition ice nucleation and immersion freezing potential of amorphous secondary organic aerosol: Pathways for ice and mixed-phase cloud formation, Journal of Geophysical Research: Atmospheres, 117, https://doi.org/https://doi.org/10.1029/2012JD018063, 2012.

695 Westbrook, C. D., Hogan, R. J., and Illingworth, A. J.: The Capacitance of Pristine Ice Crystals and Aggregate Snowflakes, Journal of the Atmospheric Sciences, 65, 206 – 219, https://doi.org/10.1175/2007JAS2315.1, 2008.

Wolf, M., Zhang, Y., Zawadowicz, M., Goodell, M., Froyd, K., Freney, E., Sellegri, K., Rösch, M., Cui, T., Winter, M., Lacher, L., Axisa, D., Axisa, D., DeMott, P. J., Levin, E., T., J., Gute, E., Abbatt, J., Koss, A., Kroll, J. H., Surratt, J. D., and Cziczo, D. J.: A biogenic secondary organic aerosol source of cirrus ice nucleating particles, Nature Communications, 11, https://doi.org/10.1038/s41467-020-18424-6, 2020.